nature cell biology

The cilia protein IFT88 is required for spindle orientation in mitosis

Benedicte Delaval[1], Alison Bright[1], Nathan D. Lawson[2] and Stephen Doxsey[1,3]

Cilia dysfunction has long been associated with cyst formation and ciliopathies[1]. More recently, misoriented cell division has been observed in cystic kidneys[2], but the molecular mechanism leading to this abnormality remains unclear. Proteins of the intraflagellar transport (IFT) machinery are linked to cystogenesis and are required for cilia formation in non-cycling cells[3,4]. Several IFT proteins also localize to spindle poles in mitosis[5–8], indicating uncharacterized functions for these proteins in dividing cells. Here, we show that IFT88 depletion induces mitotic defects in human cultured cells, in kidney cells from the IFT88 mouse mutant *Tg737*^{orpk} and in zebrafish embryos. In mitosis, IFT88 is part of a dynein1-driven complex that transports peripheral microtubule clusters containing microtubule-nucleating proteins to spindle poles to ensure proper formation of astral microtubule arrays and thus proper spindle orientation. This work identifies a mitotic mechanism for a cilia protein in the orientation of cell division and has important implications for the etiology of ciliopathies.

In non-cycling cells, centrosomes (basal bodies) contribute to the assembly of primary cilia[9] through intraflagellar transport, an intracellular motility system in which protein complexes are transported bidirectionally along the cilium[10–12]. During mitosis, centrosomes (spindle poles) participate in the organization and orientation of the spindle[13–15]. In this context, astral microtubules interact with spindle microtubules to facilitate chromosome segregation[13] and with the cell cortex to orient the spindle[14,15]. One of the best-studied IFT proteins, IFT88, which was first characterized for its role in cilia formation and polycystic kidney disease[3,16–19], also localizes to spindle poles during mitosis[6].

To test for mitotic functions of IFT88, the protein was depleted in several experimental systems. In HeLa cells, defects in mitosis were first indicated by an increased mitotic index and delayed mitotic progression (Supplementary Fig. S1a–e). Closer inspection revealed spindle pole disruption, chromosome misalignment and spindle misorientation (Fig. 1a,b). The spindle angle relative to the cell–substrate adhesion plane[15] (Fig. 1c,d) of most IFT88-depleted cells (~80%) was greater than 10°, whereas control spindles were usually parallel to the substratum (Fig. 1d), demonstrating a critical role for IFT88 in spindle orientation. Time-lapse microscopy imaging showed that spindle misorientation resulted in misoriented cell divisions, where one daughter cell divided outside the plane of the substratum, thus delaying adherence to the substrate (Fig. 1e,f). Despite misorientation, spindles were largely bipolar (Fig. 1a) and cells ultimately progressed through division (Fig. 1f and Supplementary Fig. S1d). Given the role of IFT88 in cystic kidney formation[3], IFT88 disruption was examined in kidney cell lines by siRNA (porcine LLC-PK1; Supplementary Fig. S2a–c) and by mutation (murine *Tg737*^{orpk}; Fig. 1g and Supplementary Fig. S2d) and showed similar mitotic defects. In zebrafish embryos, IFT88 depletion by morpholino oligonucleotides known to induce ciliopathies[18] also resulted in mitotic defects including misoriented spindles (Fig. 1h and Supplementary Fig. S2e). These results demonstrate a conserved mitotic role for IFT88 in spindle and cell-division orientation.

We next examined the structural underpinnings of spindle misorientation induced by IFT88 depletion. The most notable defect was a significant loss and shortening of astral microtubules, which did not contact the cell cortex, a requirement for force generation during spindle orientation (Fig. 2a,b). This phenotype was consistently observed in different experimental systems (Figs 1g and 2a,b), demonstrating a conserved role for IFT88 in the formation of astral microtubule arrays.

In centrosome-containing cells, astral microtubule arrays arise from both centrosome-based nucleation and transport of microtubule clusters to the poles from the periphery[20,21]. To define the role of IFT88 in the assembly of astral microtubule arrays, we tested the contribution of the protein in both processes. A role for IFT88 in microtubule nucleation was first indicated by loss of microtubule-nucleating components, γ-tubulin and end-binding protein 1 (EB1; refs 13, 22–25) from spindle poles following IFT88 depletion (Fig. 2c,d and

[1]Program in Molecular Medicine, University of Massachusetts Medical School, 373 Plantation Street, Suite 210, Worcester, Massachusetts 01605, USA. [2]Program in Gene Function and Expression, University of Massachusetts Medical School, Worcester, Massachusetts 01605, USA.
[3]Correspondence should be addressed to S.D. (e-mail: Stephen.Doxsey@umassmed.edu)

Received 5 November 2010; accepted 4 January 2011; published online 27 March 2011; DOI: 10.1038/ncb2202

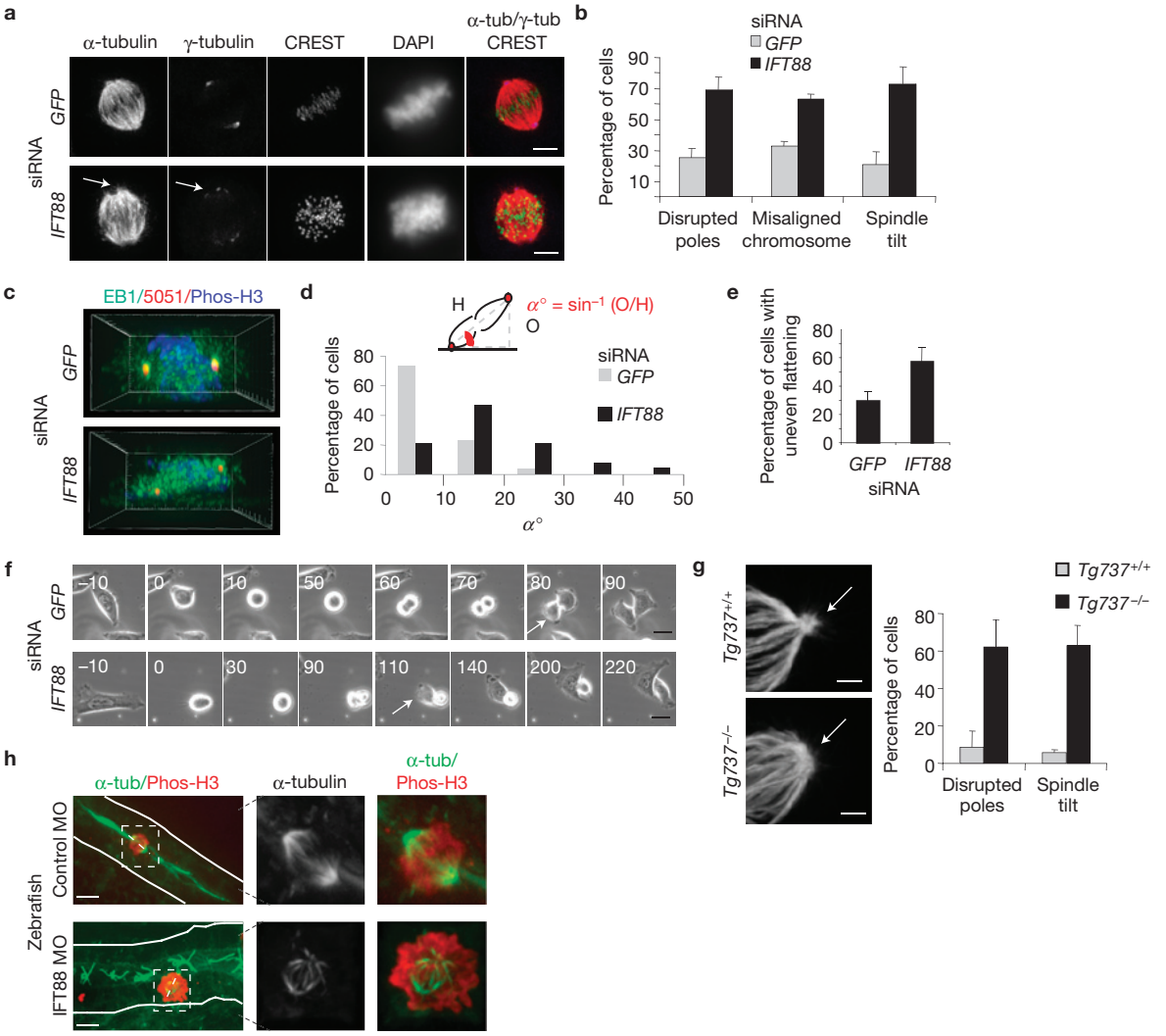

Figure 1 IFT88 depletion leads to mitotic defects in HeLa cells, kidney cells from the *Tg737*^{orpk} mouse mutant and zebrafish. (**a**) Immunofluorescence microscopy images of control (*GFP*) and *IFT88*-siRNA-treated mitotic HeLa cells. α-tubulin (microtubules) and γ-tubulin (spindle poles, arrow) staining show spindle pole defects. CREST (kinetochores) or DAPI (DNA) staining shows misaligned chromosomes. Scale bars, 5 μm. (**b**) Quantification of mitotic defects following *IFT88*- or control (*GFP*)-siRNA treatment in HeLa cells. Defects include disrupted poles (α- and γ-tubulin), misaligned chromosomes (DAPI staining) and spindle misorientation (spindle tilt, spindle poles in different focal planes). $n = 70$ mitotic cells per experiment. (**c**) Side views of 3D reconstructed immunofluoresence images showing misoriented mitotic spindles in *IFT88*- versus control-siRNA-treated HeLa cells. Spindle (EB1), centrosomes (5051) and DNA (Phos-H3). (**d**) Histogram showing metaphase spindle-angle distribution in control- and *IFT88*-siRNA-treated cells. $n = 30$ mitotic spindles. Schematic (top) showing spindle angle (α) measurement. H, hypotenuse. O, opposite. (**e**,**f**) Quantification (**e**) and time-lapse microscopy images (**f**) showing uneven timing of daughter-cell flattening onto the substrate after mitosis (misoriented cell division) in *IFT88*-siRNA-treated HeLa cells, compared with control. $n = 50$ mitotic cells per experiment. Arrows, time when the first daughter cell begins flattening. Time, min. Scale bar, 10 μm. (**g**) Immunofluorescence microscopy images (left) showing a disrupted spindle pole (α-tubulin, arrow) in kidney cells derived from the IFT88 mouse mutant *Tg737*^{orpk} (*Tg737*$^{-/-}$), compared with wild type (*Tg737*$^{+/+}$). Scale bars, 2 μm. Graph (right), quantification of mitotic defects in wild-type and *Tg737*^{orpk} mutant cells. (**h**) Immunofluorescence microscopy images of mitotic spindles from the pronephric ducts of whole-mount zebrafish embryos. Control embryo, cell with aligned chromosomes and mitotic spindle oriented in the longitudinal plane of the duct. IFT88-depleted embryo, cell with non-aligned chromosomes and misoriented spindle. Lines, pronephric duct border. Dashed lines, spindle orientation. MO, morpholino. Right, enlargements of spindles outlined by dashed rectangles. Scale bar, 5 μm.

Supplementary Fig. S3a,b); EB1 depletion did not affect IFT88 pole localization (Supplementary Fig. S3c). The similarities in mitotic phenotypes induced by depletion of IFT88, EB1 or γ-tubulin (spindle pole defects, reduced astral microtubules and misoriented spindle; Fig. 1; refs 15,23–25) and the mitotic interaction of IFT88 with EB1 and γ-tubulin (Fig. 2e) supported the idea that these proteins may co-function in mitosis. More specifically, the impaired recruitment of γ-tubulin to spindle poles in IFT88-depleted cells following microtubule regrowth (Fig. 2f) indicated a role for IFT88 in the recruitment of microtubule-nucleating components to spindle poles. Consistent with the polar loss of microtubule-nucleating proteins, IFT88 depletion decreased microtubule nucleation, but the effect was modest when compared with the marked disruption of astral microtubules (Fig. 2g,h and Supplementary Fig. S3d). This observation and the known role of IFT proteins in the transport of components in cilia[10,11] indicated that IFT88 might function in microtubule transport to poles during mitosis rather than directly participating in microtubule nucleation at poles.

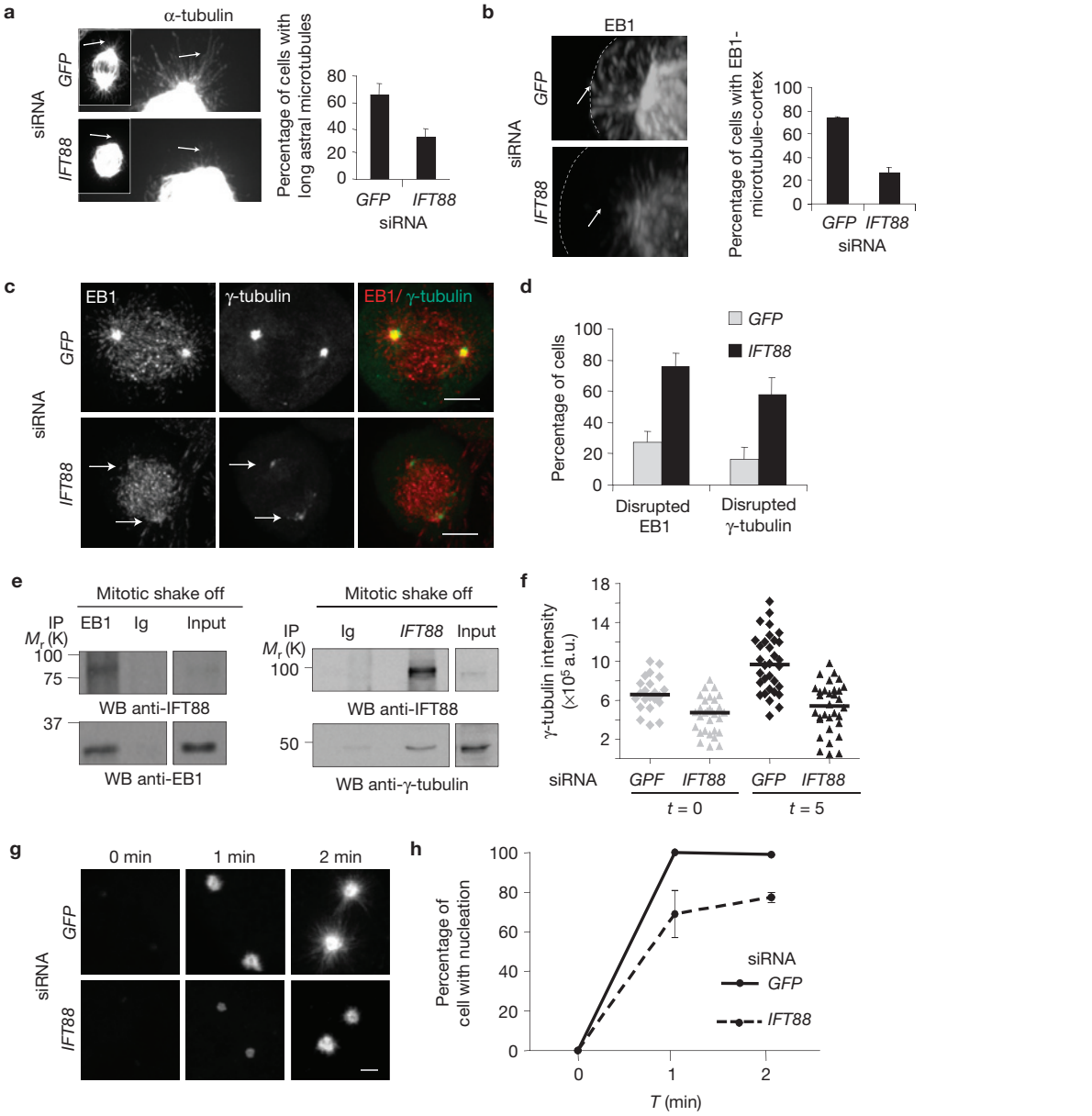

Figure 2 IFT88 depletion disrupts astral microtubules and the spindle pole localization of proteins involved in microtubule nucleation in HeLa cells. (**a**) Immunofluoresence microscopy images (left) of mitotic spindles showing disrupted astral microtubules (α-tubulin) at spindle poles of IFT88-depleted cells, compared with control. Pixel intensity range increased to visualize astral microtubules (arrow). Enlargements, spindle pole region. Graph (right), quantification of cells with long astral microtubules (>3 μm). $n = 70$ mitotic spindles per experiment. (**b**) Side view of 3D reconstructed images (left) showing astral microtubules (EB1 staining) contacting the cortex in control cells (arrow, upper panel) and astral microtubules that fail to contact the cell cortex in IFT88-depleted cells (arrow, lower panel). Dotted lines, cell cortex. Graph (right), quantification of cells with both poles showing astral microtubules contacting cortex. $n = 50$ mitotic spindles per experiment. (**c**,**d**) Immunofluorescence microscopy images (**c**) and quantification (**d**) of mitotic spindles showing loss of EB1 and γ-tubulin from spindle poles (arrow) in IFT88-depleted cells, compared with control. Graph (**d**), percentage of cells with disrupted pole localization of EB1 or γ-tubulin. $n = 50$ mitotic spindles per experiment. Scale bar, 5 μm. (**e**) Immunoblots (WB) showing that IFT88 co-immunoprecipitates with EB1 (left) and that γ-tubulin co-immunoprecipitates with IFT88 (right) from lysates of mitotic HeLa cells, demonstrating a mitotic interaction between the proteins, either direct or indirect. Ig, rabbit antibody, negative immunoprecipitation (IP) control. Input, 5% of total lysate used for immunoprecipitation. For full scan of immunoblots, see Supplementary Fig. S8. (**f**) Quantification of γ-tubulin intensity at spindle poles of mitotic cells showing γ-tubulin recruitment to poles in a microtubule regrowth experiment. *t*, time after nocodazole washout (min). Bar, median. Experiment shown is representative of three independent experiments. a.u., arbitrary unit. (**g**) Immunofluoresence microscopy images showing microtubule regrowth (α-tubulin) at mitotic spindle poles 0, 1 and 2 min after nocodazole washout in IFT88- or GFP-depleted mitotic cells. $t = 0$ min shows no nucleation in GFP- and IFT88-depleted cells, and $t = 1$ min and 2 min show decreased nucleation in IFT88-depleted cells, compared with control cells. Scale bar, 2 μm. (**h**) Percentage of cells showing detectable nucleation (aster size ≥1 μm) 0, 1 and 2 min after nocodazole washout. $n = 50$ mitotic cells per experiment; error bars, mean of at least three experiments ± s.d.

To test this, we examined the role of IFT88 in the transport of peripheral microtubule clusters towards spindle poles during the prophase-to-metaphase transition using green fluorescent protein (GFP)–α-tubulin-expressing LLC-PK1 cells previously optimized for

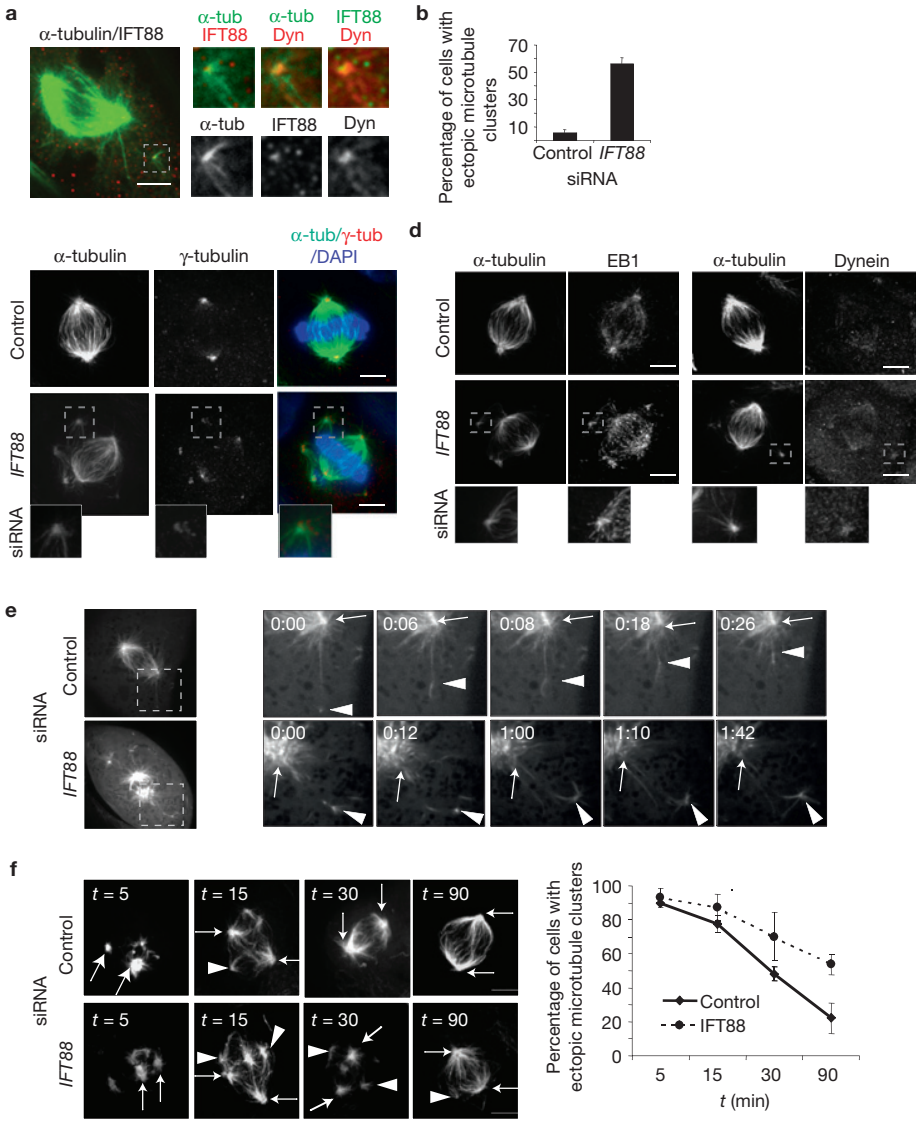

Figure 3 IFT88 is required for the movement of peripheral microtubule clusters containing microtubule-nucleating components towards spindle poles in LLC-PK1 cells stably expressing GFP–α-tubulin. (**a**) Immunofluoresence microscopy images showing IFT88 and dynein intermediate chain (Dyn) localizing to a peripheral microtubule cluster (GFP–α-tubulin) in a prometaphase cell. Pixel intensity range increased to visualize peripheral microtubule cluster. Scale bar, 5 μm. Inset, peripheral microtubule cluster. See Supplementary Fig. S4a for negative controls. (**b**) Quantification of GFP–α-tubulin LLC-PK1 metaphase cells with ectopic microtubule clusters following *IFT88*- or control- (lamin) siRNA treatment. $n = 50$ mitotic cells per experiment. (**c**,**d**) Immunofluoresence microscopy images of GFP–α-tubulin LLC-PK1 control or IFT88-depleted metaphase cells. γ-tubulin (**c**), EB1 (**d**, left) and dynein (**d**, right) localize to ectopic microtubule clusters. Insets, ectopic microtubule clusters. Scale bar, 5 μm. (**e**) Selected still images from time-lapse microscopy movies of GFP–α-tubulin LLC-PK1 cells. Control prometaphase, minus-end-directed motion of peripheral microtubule clusters towards spindle pole. In IFT88-depleted cells, peripheral clusters formed, but showed no movement towards spindle poles. Full cell (left); enlargement of spindle pole and microtubule cluster (right). Time (min); arrowhead, microtubule cluster; arrow, spindle pole. (**f**) Immunofluorescence microscopy images (left) and quantification (right) of the relocalization of microtubule clusters to spindle poles in a spindle reassembly assay (α-tubulin, microtubule regrowth following nocodazole washout). The decrease in cells with ectopic microtubule clusters over time correlates with their movement towards the poles. IFT88 depletion delays relocalization of microtubule clusters to poles. Arrows, spindle poles (localization confirmed with centrosome protein staining). Arrowheads, ectopic microtubule clusters. $n = 40$ mitotic cells per experiment per time point. t, time after nocodazole washout (min).

this purpose[21]. In prometaphase, IFT88 localized to foci at the minus end of peripheral microtubule clusters where the dynein motor was previously localized[21] (Fig. 3a and Supplementary Fig. S4a). In IFT88-depleted cells, peripheral microtubule clusters accumulated in the cytoplasm (Fig. 3b), indicating that they were unable to integrate into spindle poles during the prometaphase-to-metaphase transition. The ectopic microtubule clusters contained the microtubule-nucleating proteins γ-tubulin and EB1, and the microtubule-associated motor dynein1 (Fig. 3c,d). To directly test whether IFT88 is required for the movement of microtubule clusters, we examined the recruitment of peripheral microtubules to poles by time-lapse microscopy imaging (Fig. 3e; Supplementary Movies S1–S4). In control cells, peripheral microtubules moved poleward in prometaphase and contributed to the formation of robust spindle poles, as seen previously[20,21]

(Fig. 3e top panel and Supplementary Movie S1). By metaphase, most clusters were cleared from the periphery and incorporated into spindle poles (Supplementary Movie S2). In IFT88-depleted cells, peripheral microtubule clusters did not move towards spindle poles in prometaphase (Fig. 3e lower panel and Supplementary Movie S3) and by metaphase, they were still not cleared from the periphery (Supplementary Movie S4), indicating a defect in transport. An independent strategy that directly tests the movement of microtubule clusters from periphery to poles during spindle reassembly[26] also revealed a defect in relocalization of microtubule clusters to poles following IFT88 depletion (Fig. 3f). These results uncover a new role for IFT88 in the movement and subsequent integration of microtubule clusters containing microtubule-nucleating proteins into spindle poles. They further indicate that IFT88 may be part of a transport complex in mitosis.

Microtubule cluster transport towards spindle poles requires the minus-end-directed motor dynein1 (ref. 21). In cilia, the movement of IFT88-containing particles is also motor dependent[11]. We thus investigated whether IFT88 was part of a microtubule-based, motor-driven transport system in mitosis as it is in ciliated cells. Consistent with this model, IFT88 co-pelleted with taxol-stabilized microtubules from mitotic cell lysates (Fig. 4a). Moreover, the spindle pole localization of IFT88 was dependent on microtubules, as shown by the marked reduction of IFT88 at spindle poles following microtubule depolymerization, and its restoration after nocodazole washout (Fig. 4b). During spindle reassembly, a remarkable redistribution of IFT88 was observed. Within 5 min, IFT88 redistributed from a diffuse cytoplasmic location to numerous cytoplasmic foci (Fig. 4b). The IFT88 foci contained α-tubulin and singular or bundled microtubules as well as the newly characterized IFT88 mitotic interacting partners, γ-tubulin and EB1 (Fig. 4c,d). With time, the number of IFT88 foci decreased concomitant with an increase in the spindle pole fraction (Fig. 4e), indicative of translocation of the cytoplasmic foci to poles. Direct translocation of IFT88 to spindle poles was tested using GFP–IFT88-expressing LLC-PK1 cells (Fig. 4f). GFP–IFT88 localized to spindle poles and to cytoplasmic foci, confirming results with the endogenous protein. GFP–IFT88 foci exhibited vectorial movement towards poles (Fig. 4f and Supplementary Movie S5); anterograde movements were also observed (Fig. 4f, right). The speed of IFT88 retrograde movement ($>1\,\mu m\,s^{-1}$) was consistent with dynein-mediated motility, indicating that polar transport of IFT88 was mediated by dynein (Fig. 4f, right), possibly in the form of a dynein–IFT88 complex. The common functions of IFT88 and dynein1 in astral microtubule organization, mitotic spindle orientation[14,27–29] (Figs 1 and 2a,b) and transport of microtubule clusters[21] (Fig. 3) supported this model.

To directly test for the presence of a mitotic IFT88 transport complex, we carried out a series of biochemical experiments. The approximate size of mitotic IFT88 complexes was determined by gel filtration chromatography (Fig. 5a). IFT88 was detected in fractions 16–20 (relative molecular mass M_r∼2,000K–5,000K), where it partially co-eluted with dynein1; a separate peak of IFT88 appeared in fraction 26 (M_r of ∼600K). Dynein co-eluted with dynactin components (fractions 16–22), indicating that the integrity of the dynein–dynactin complex was retained during gel filtration chromatography (Fig. 5a). The partial co-elution of IFT88 and dynein indicated that a subfraction of IFT88 may interact with a subfraction of dynein in a large M_r∼2,000K–5,000K complex (Fig. 5a). In fact, IFT88 and dynein co-immunoprecipitated from mitotic lysates (Supplementary Fig. S4b,c). Immunoprecipitation experiments carried out on gel-filtration-chromatography fractions containing dynein confirmed that the interaction was maintained after gel filtration chromatography (Fig. 5a, right), providing further evidence for an IFT88–dynein1 complex in mitosis. Additional IFT proteins co-eluted with IFT88 in the M_r∼2, 000K–5, 000K range and an interaction between IFT88 and IFT52 (another IFT B-complex component) was identified in mitotic cells (Fig. 5a and Supplementary Fig. S4d,e). These data indicate that IFT88 and maybe other IFT proteins are part of a large dynein1-containing protein complex during mitosis.

To test for a role of dynein1 in the spindle pole localization of IFT88, dynein1 heavy chain was depleted by siRNA. An increase in mitotic index[29] and interphase defects[30] were observed (Supplementary Fig. S5), validating the efficacy of the siRNA. In addition, dynein1 depletion induced a unique redistribution of IFT88 from its focused spindle pole position to a more diffuse region surrounding the poles (Fig. 5b–d), but did not markedly affect the centrosome localization of IFT88 in interphase as previously reported[6] (Supplementary Fig. S6a). The IFT88 localization pattern was unlike other spindle pole proteins, which were lost from poles but not redistributed (Supplementary Fig. S6b). This observation and the fact that IFT88 mislocalization occurred before major spindle disruption (Supplementary Fig. S6c,d), indicated that IFT88 mislocalization was not due to global perturbations of the spindle. The mitotic redistribution of IFT88 following dynein1 depletion was reminiscent of IFT88 accumulation at cilia tips following depletion of the cilia-associated dynein2 motor[12], an apparent consequence of net microtubule plus-end motor activity in the absence of minus-end activity (Fig. 5d). A similar redistribution of IFT88 was observed following depletion of p50 dynactin, which disrupts dynein function[29] (Supplementary Fig. S6e–g). In contrast, depletion of the dynein2 motor, which is required for retrograde transport in cilia[11,12], did not affect mitotic index, spindle organization or the spindle pole localization of IFT88, despite its robust interphase and ciliary phenotypes[31] (Supplementary Figs S5 and S7). These data demonstrate a role for cytoplasmic dynein1 in the microtubule-dependent spindle pole localization of IFT88 and indicate that IFT88 functions as part of a previously uncharacterized dynein1-driven complex in mitotic cells.

To directly test the role of dynein1 in IFT88 transport to spindle poles, we examined the translocation of IFT88 foci from cytoplasm to poles during spindle reassembly (Fig. 5e,f). In dynein-depleted cells, IFT88 foci were delayed in their relocalization, as demonstrated by an increase in the number of IFT88 foci remaining in the cytoplasm after microtubule regrowth and a decrease in IFT88 at spindle poles (Fig. 5e). More specifically, 30 min after nocodazole washout, most control cells (85%) lacked cytoplasmic foci and showed IFT88 at poles, whereas half of the dynein1-depleted cells still showed cytoplasmic IFT88 foci and weak pole staining (Fig. 5f). This demonstrates that dynein1 is required for the transport of IFT88 to spindle poles.

This work identifies a role for an IFT protein in the formation of mitotic astral microtubule arrays and thus establishes a new molecular mechanism for a cilia protein in spindle orientation. These results, together with the previously established role of dynein1 in transporting peripheral microtubules[21] and centrosome components[32]

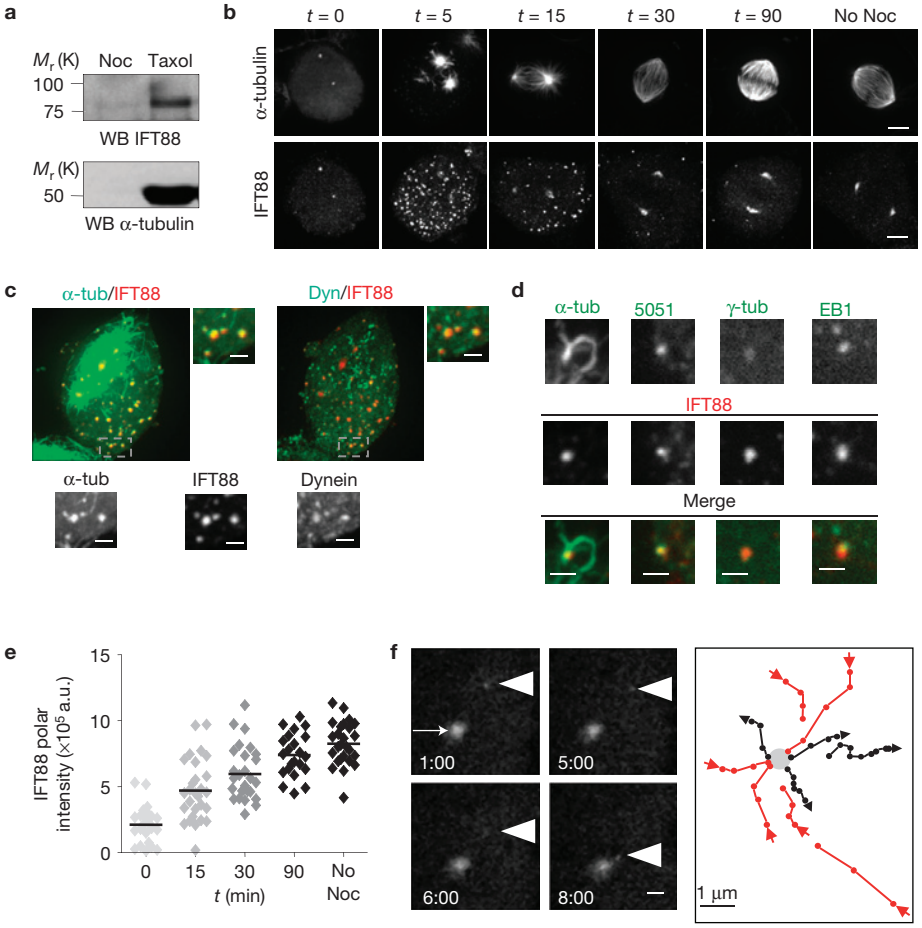

Figure 4 IFT88 moves towards spindle poles and requires microtubules for its spindle pole localization. (**a**) Microtubule pulldown assay shows that IFT88 co-pelleted with taxol-stabilized microtubules in mitotic HeLa cell lysates. Nocodazole (Noc), inhibition of microtubule polymerization used as negative control. α-tubulin, microtubules. (**b**) Immunofluoresence microscopy images showing IFT88 foci formation (lower panel) after nocodazole washout (α-tubulin, microtubule regrowth; upper panel) in HeLa cells. *t*, time after nocodazole washout (min). Control without nocodazole (no Noc). Scale bar, 5 μm. (**c**,**d**) Immunofluorescence microscopy images showing the molecular composition of IFT88 foci in HeLa cells. Maximum projection of a cell with IFT88 foci 5 min after nocodazole washout (**c**) showing that IFT88 foci co-stain for α-tubulin (α-tub) and dynein intermediate chain (Dyn). Enlargements, single plane of the outlined foci. Enlargements of IFT88 foci (**d**) showing that microtubule clusters (α-tubulin; α-tub) can be observed extending from some foci, and that IFT88 foci co-stain with microtubule-nucleating components (5051, centrosome protein marker; γ-tubulin; EB1). Pixel intensity range increased to visualize foci. Scale bar, 1 μm. (**e**) Quantification of IFT88 intensity at spindle poles of mitotic HeLa cells showing IFT88 recruitment to poles following nocodazole washout. *t*, time after nocodazole washout (min). Experiment shown is representative of three independent experiments. Bar, median. a.u., arbitrary unit. No nocodazole (No Noc), untreated cells. (**f**) Still images from time-lapse microscopy imaging of a GFP–IFT88 LLC-PK1 cell line (left) showing one of the GFP–IFT88 foci (arrowhead) moving towards the GFP–IFT88-labelled spindle pole (arrow). Time elapsed is shown in seconds. Scale bar, 1 μm. Schematic representation (right) of several GFP–IFT88 foci moving towards (red arrow) or away from (black arrowhead) the spindle pole (grey dot). Time between points, 1 s. Arrows indicate the direction of the movement.

to spindle poles, indicate that an IFT88–dynein1 complex transports peripheral microtubule clusters and associated microtubule-nucleating components to spindle poles (Fig. 5g). These microtubule clusters can be viewed as 'pre-fabricated' parts of the spindle pole, an observation reminiscent of 'pre-assembled' cilia components transported by motors along the cilia[11]. Integration of microtubule clusters into spindle poles instantly contributes to the astral microtubule population and the microtubule-nucleating components present in these structures (γ-tubulin, EB1) could contribute to microtubule nucleation at poles. Collectively, these events facilitate formation of astral microtubule arrays and subsequently spindle orientation. The IFT88-mediated spindle pole assembly pathway provides new insight into the underpinnings of fundamental processes including cystogenesis and asymmetric cell division[33].

As cilia disassemble before mitotic entry and HeLa cells are considered non-ciliated[34], the role of IFT88 in the formation of mitotic astral microtubule arrays represents a previously unknown cilia-independent function for this protein, in addition to its role in cilia formation[3], cell-cycle progression[6] and membrane trafficking[35]. The spindle pole localization of several other IFT proteins[5–8] and the mitotic interaction between IFT52 and IFT88 (Supplementary Fig. S4d,e) indicate that other IFT proteins, and maybe other classes of cilia proteins, may function in dividing cells. Moreover, the anterograde movement of IFT88 foci is indicative of a role for microtubule plus-end-directed motors in IFT88 mitotic transport (Figs 4f and 5d).

IFT88 depletion primarily affects a subset of microtubules in mitosis (astrals), consistent with the selective disruption of spindle function. The observed delay in mitosis, rather than a complete mitotic

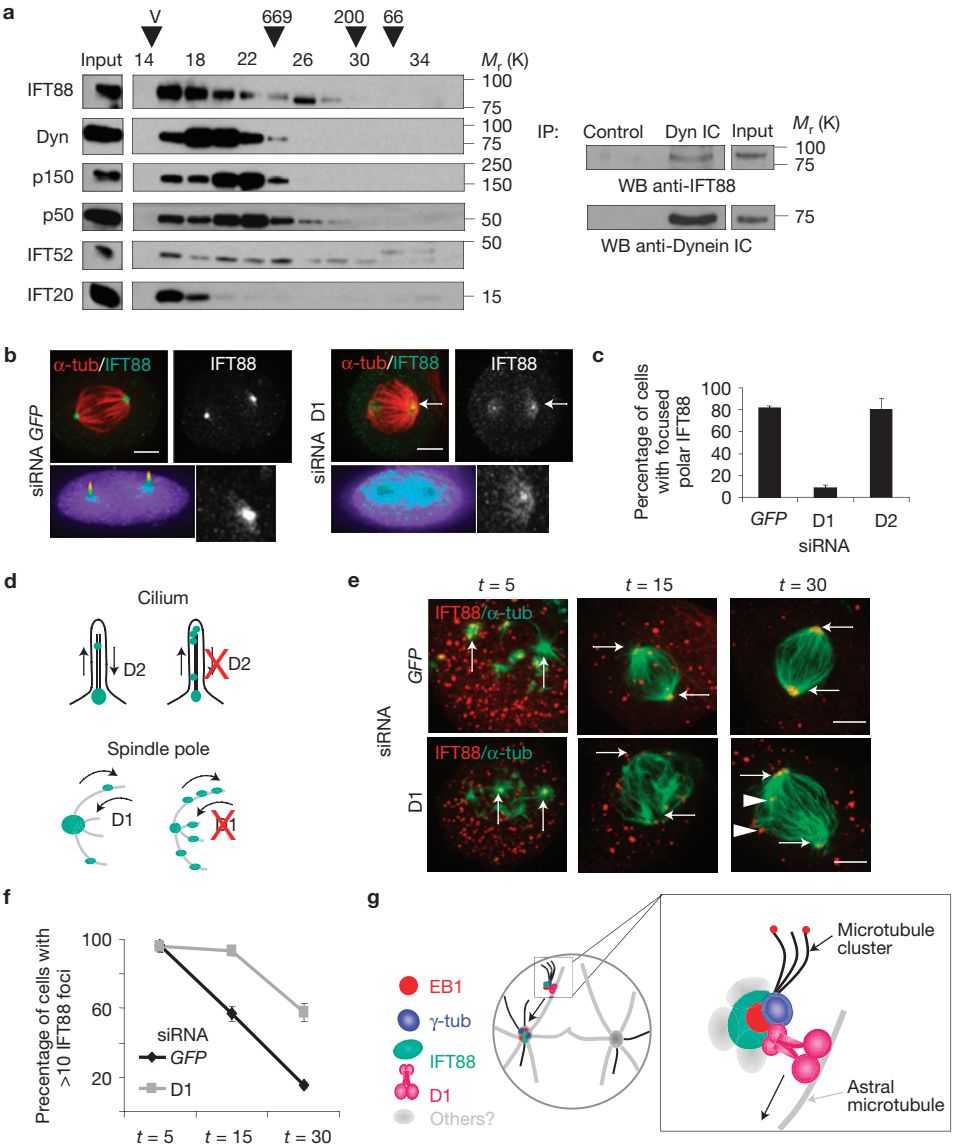

Figure 5 IFT88 is part of a dynein1-driven transport complex in mitosis. (**a**) Immunoblots (left) showing fractions of mitotic HeLa cell lysates obtained after gel-filtration fractionation and probed for IFT88, dynein intermediate chain (Dyn IC), dynactin p150/glued, p50 dynactin, IFT52 and IFT20. Input, total lysate before gel filtration chromatography. Arrowheads, peak elution fraction for calibration proteins: bovine serum albumin (M_r 66K), β-amylase (M_r 200K), thyroglobulin (M_r 669K). V, Void volume. Immunoprecipitation experiment (right) carried out on fractions 16–22 from gel filtration containing dynein. Immunoblots show that IFT88 co-immunoprecipitates with dynein (IC, intermediate chain) after gel filtration chromatography. For full scan of immunoblots, see Supplementary Fig. S8. (**b**) Immunofluorescence microscopy images of HeLa cells showing IFT88 redistribution from mitotic spindle poles to a more diffuse region surrounding the poles following dynein1 (D1) depletion, compared with control (GFP). α-tubulin; α-tub. Intensity profiles, lower left panels; spindle pole enlargement, lower right panels. Scale bar, 5 μm. (**c**) Percentage of cells with focused IFT88 localization at poles following *dynein1*- (D1) or *dynein2*- (D2) siRNA treatment. $n = 70$ mitotic spindles per experiment. (**d**) Schematic representation of IFT88 (green) redistribution in cilia when dynein2 (D2) is depleted, and around mitotic spindle poles when dynein1 (D1) is depleted. (**e**) Immunofluorescence microscopy images showing that D1 depletion in HeLa cells delays IFT88 (red) relocalization to spindle poles in a spindle reassembly assay (α-tubulin, green). The decrease of cytoplasmic foci over time, observed in control (GFP) cells correlates with the relocalization of IFT88 from foci to spindle poles. Despite the formation of microtubule clusters in D1-depleted cells, several IFT88 foci remain in the cytoplasm 30 min after nocodazole washout. Arrows, spindle poles; arrowheads, IFT88 foci. (**f**) Percentage of cells with more than ten cytoplasmic foci. $n = 40$ cells per experiment per time point. *t*, time after nocodazole washout (min). (**g**) Molecular model for IFT88 function in mitosis. IFT88 is depicted as a component of a minus-end-directed dynein1-driven transport complex. This complex is required for transport of microtubule clusters and their associated nucleating components (EB1 and γ-tubulin) to spindle poles. IFT88 thus contributes to the formation of astral microtubule arrays and consequently spindle orientation. Adapted from ref. 20.

block, indicates that there are no major, potentially fatal defects in spindle function. IFT88 may thus operate selectively in cells, tissues and organisms that require astral microtubules for proper spindle orientation, such as the oriented cell divisions in an epithelial layer or the asymmetric division of stem cells[33]. This may explain why IFT88 disruption is not associated with more severe phenotypes in mouse, *Drosophila* or *Caenorhabditis elegans* embryos, such as lethality in the earliest embryonic stages[16,17,19].

Cystogenesis has been associated with cilia disruption and misoriented cell division[2]. Despite the appeal for a role of cilia in regulating the planar cell polarity[36], the molecular mechanism leading to misoriented cell division remains unclear. This work provides a likely mechanism for IFT88 function in oriented cell divisions. Further work is required to test whether the pathway outlined here for IFT88 can be applied to other cilia proteins involved in cystogenesis. □

METHODS

Methods and any associated references are available in the online version of the paper at http://www.nature.com/naturecellbiology/

Note: Supplementary Information is available on the Nature Cell Biology website

ACKNOWLEDGEMENTS

We thank G. Pazour, G. Witman and P. Wadsworth for thoughtful discussions on this work, and S. Redick for assistance with microscopy. We are particularly grateful to L. Covassin-Barberis in N.L. laboratory and N.L. Adkins in C. Peterson's laboratory for guidance on zebrafish experimental work and gel-filtration experiments, respectively. We thank G. Pazour for the gift of IFT88 antibody and GFP–IFT88 LLC-PK1, Flag–IFT52 IMCD stable cell lines, P. Wadsworth for the GFP–α-tubulin LLC-PK1 cell line and C. Desdouets, P. Denoulet and C. Janke for their gift of antibodies specific to IFT88 and polyglutamylated tubulin, respectively. Core resources supported by the Diabetes Endocrinology Research Center grant DK32520 were used; S.D. is a member of the UMass DERC (DK32520). This work was supported by financial support from the National Institutes of Health (GM51994) to S.D. and the Polycystic Kidney Disease Foundation to B.D.

AUTHOR CONTRIBUTIONS

B.D. and S.D. wrote the manuscript. B.D. conceived and planned the experimental work. B.D. and A.B. carried out the experimental work and analysed the data. N.D.L. provided the zebrafish facility and helped plan and guide the zebrafish experimental work.

COMPETING FINANCIAL INTERESTS

The authors declare no competing financial interests.

Published online at http://www.nature.com/naturecellbiology
Reprints and permissions information is available online at http://npg.nature.com/reprintsandpermissions/

1. Hildebrandt, F. & Otto, E. Cilia and centrosomes: a unifying pathogenic concept for cystic kidney disease?. *Nat. Rev. Genet.* **6,** 928–940 (2005).
2. Fischer, E. *et al.* Defective planar cell polarity in polycystic kidney disease. *Nat. Genet.* **38,** 21–23 (2006).
3. Pazour, G. J. *et al.* *Chlamydomonas* IFT88 and its mouse homologue, polycystic kidney disease gene tg737, are required for assembly of cilia and flagella. *J. Cell Biol.* **151,** 709–718 (2000).
4. Sun, Z. *et al.* A genetic screen in zebrafish identifies cilia genes as a principal cause of cystic kidney. *Development* **131,** 4085–4093 (2004).
5. Iomini, C., Tejada, K., Mo, W., Vaananen, H. & Piperno, G. Primary cilia of human endothelial cells disassemble under laminar shear stress. *J. Cell Biol.* **164,** 811–817 (2004).
6. Robert, A. *et al.* The intraflagellar transport component IFT88/polaris is a centrosomal protein regulating G1-S transition in non-ciliated cells. *J. Cell Sci.* **120,** 628–637 (2007).
7. Follit, J. A., Tuft, R. A., Fogarty, K. E. & Pazour, G. J. The intraflagellar transport protein IFT20 is associated with the Golgi complex and is required for cilia assembly. *Mol. Biol. Cell* **17,** 3781–3792 (2006).
8. Deane, J. A., Cole, D. G., Seeley, E. S., Diener, D. R. & Rosenbaum, J. L. Localization of intraflagellar transport protein IFT52 identifies basal body transitional fibers as the docking site for IFT particles. *Curr. Biol.* **11,** 1586–1590 (2001).
9. Rieder, C. L., Faruki, S. & Khodjakov, A. The centrosome in vertebrates: more than a microtubule-organizing centre. *Trends Cell Biol.* **11,** 413–419 (2001).
10. Scholey, J. M. Intraflagellar transport motors in cilia: moving along the cell's antenna. *J. Cell Biol.* **180,** 23–29 (2008).
11. Rosenbaum, J. L. & Witman, G. B. Intraflagellar transport. *Nat. Rev. Mol. Cell Biol.* **3,** 813–825 (2002).
12. Pazour, G. J., Dickert, B. L. & Witman, G. B. The DHC1b (DHC2) isoform of cytoplasmic dynein is required for flagellar assembly. *J. Cell Biol.* **144,** 473–481 (1999).
13. Luders, J. & Stearns, T. Microtubule-organizing centres: a re-evaluation. *Nat. Rev. Mol. Cell Biol.* **8,** 161–167 (2007).
14. O'Connell, C. B. & Wang, Y. L. Mammalian spindle orientation and position respond to changes in cell shape in a dynein-dependent fashion. *Mol. Biol. Cell* **11,** 1765–1774 (2000).
15. Toyoshima, F. & Nishida, E. Integrin-mediated adhesion orients the spindle parallel to the substratum in an EB1- and myosin X-dependent manner. *EMBO J.* **26,** 1487–1498 (2007).
16. Murcia, N. S. *et al.* The Oak Ridge Polycystic Kidney (orpk) disease gene is required for left-right axis determination. *Development* **127,** 2347–2355 (2000).
17. Haycraft, C. J., Swoboda, P., Taulman, P. D., Thomas, J. H. & Yoder, B. K. The *C. elegans* homolog of the murine cystic kidney disease gene Tg737 functions in a ciliogenic pathway and is disrupted in osm-5 mutant worms. *Development* **128,** 1493–1505 (2001).
18. Kramer-Zucker, A. G. *et al.* Cilia-driven fluid flow in the zebrafish pronephros, brain and Kupffer's vesicle is required for normal organogenesis. *Development* **132,** 1907–1921 (2005).
19. Han, Y. G., Kwok, B. H. & Kernan, M. J. Intraflagellar transport is required in *Drosophila* to differentiate sensory cilia but not sperm. *Curr. Biol.* **13,** 1679–1686 (2003).
20. Tulu, U. S., Rusan, N. M. & Wadsworth, P. Peripheral, non-centrosome-associated microtubules contribute to spindle formation in centrosome-containing cells. *Curr. Biol.* **13,** 1894–1899 (2003).
21. Rusan, N. M., Tulu, U. S., Fagerstrom, C. & Wadsworth, P. Reorganization of the microtubule array in prophase/prometaphase requires cytoplasmic dynein-dependent microtubule transport. *J. Cell Biol.* **158,** 997–1003 (2002).
22. Hannak, E. *et al.* The kinetically dominant assembly pathway for centrosomal asters in *Caenorhabditis elegans* is γ-tubulin dependent. *J. Cell Biol.* **157,** 591–602 (2002).
23. Rogers, S. L., Rogers, G. C., Sharp, D. J. & Vale, R. D. *Drosophila* EB1 is important for proper assembly, dynamics, and positioning of the mitotic spindle. *J. Cell Biol.* **158,** 873–884 (2002).
24. Zimmerman, W. C., Sillibourne, J., Rosa, J. & Doxsey, S. J. Mitosis-specific anchoring of γ tubulin complexes by pericentrin controls spindle organization and mitotic entry. *Mol. Biol. Cell* **15,** 3642–3657 (2004).
25. Green, R. A., Wollman, R. & Kaplan, K. B. APC and EB1 function together in mitosis to regulate spindle dynamics and chromosome alignment. *Mol. Biol. Cell* **16,** 4609–4622 (2005).
26. Tulu, U. S., Fagerstrom, C., Ferenz, N. P. & Wadsworth, P. Molecular requirements for kinetochore-associated microtubule formation in mammalian cells. *Curr. Biol.* **16,** 536–541 (2006).
27. Walczak, C. E., Vernos, I., Mitchison, T. J., Karsenti, E. & Heald, R. A model for the proposed roles of different microtubule-based motor proteins in establishing spindle bipolarity. *Curr. Biol.* **8,** 903–913 (1998).
28. Gaglio, T., Dionne, M. A. & Compton, D. A. Mitotic spindle poles are organized by structural and motor proteins in addition to centrosomes. *J. Cell Biol.* **138,** 1055–1066 (1997).
29. Echeverri, C. J., Paschal, B. M., Vaughan, K. T. & Vallee, R. B. Molecular characterization of the 50-kD subunit of dynactin reveals function for the complex in chromosome alignment and spindle organization during mitosis. *J. Cell Biol.* **132,** 617–633 (1996).
30. Corthesy-Theulaz, I., Pauloin, A. & Pfeffer, S. R. Cytoplasmic dynein participates in the centrosomal localization of the Golgi complex. *J. Cell Biol.* **118,** 1333–1345 (1992).
31. Vaisberg, E. A., Grissom, P. M. & McIntosh, J. R. Mammalian cells express three distinct dynein heavy chains that are localized to different cytoplasmic organelles. *J. Cell Biol.* **133,** 831–842 (1996).
32. Young, A., Dictenberg, J. B., Purohit, A., Tuft, R. & Doxsey, S. J. Cytoplasmic dynein-mediated assembly of pericentrin and γ tubulin onto centrosomes. *Mol. Biol. Cell* **11,** 2047–2056 (2000).
33. Yamashita, Y. M., Mahowald, A. P., Perlin, J. R. & Fuller, M. T. Asymmetric inheritance of mother versus daughter centrosome in stem cell division. *Science* **315,** 518–521 (2007).
34. Wheatley, D. N. Primary cilia in normal and pathological tissues. *Pathobiology* **63,** 222–238 (1995).
35. Finetti, F. *et al.* Intraflagellar transport is required for polarized recycling of the TCR/CD3 complex to the immune synapse. *Nat. Cell Biol.* **11,** 1332–1339 (2009).
36. Ross, A. J. *et al.* Disruption of Bardet-Biedl syndrome ciliary proteins perturbs planar cell polarity in vertebrates. *Nat. Genet.* **37,** 1135–1140 (2005).

METHODS

Cell culture, siRNAs and transfection. HeLa cells, hTert RPE-1 (Clontech) cells, GFP–α-tubulin LLC-PK1 stable cell line[20,21] (gift from P. Wadsworth, UMass, Amherst, USA), wild-type and *Tg737*$^{-/-}$ mouse kidney cells[37] and Flag–IFT52 IMCD (ref. 38) and GFP–IFT88 LLC-PK stable cell line (gifts from G. Pazour, UMass Medical School, USA) were grown as described by the American Type Culture Collection. Targeted proteins were depleted with small-interfering RNAs (siRNAs) designed and ordered through Dharmacon and delivered to HeLa or LLC-PK1 cells using Oligofectamine or RPE cells using Lipofectamine 2000 (Invitrogen) according to the manufacturers' instructions. Three siRNA sequences were used to target human and porcine *IFT88*: *IFT88*: 5′-CGACUAAGUGCCAGACUCAUU-3′, *IFT88#2*: 5′-CCGAAGCACUUAACACUUA-3′ previously published[6] and *IFT88sc* (*Sus Scrofa*): 5′-CCUUGGAGAUCGAGAGAAUU-3′. The efficacy of IFT88 knockdown was assessed by immunoblotting and immunofluorescence microscopy 48 h post-transfection. Functional loss of IFT88 was verified using a cilia formation assay in RPE cells[39]. A rescue experiment was carried out by depleting endogenous IFT88 (*IFT88sc* siRNA) in a porcine LLC-PK1 cell line expressing a mouse *GFP–IFT88* cDNA. *EB1* siRNA (5′-GCCCUGGUGUGGUGCGAAA-3′), *p50* siRNA (5′-GACGACAGUGAAGGAGUCAUU-3′) and siRNA specific for *dynein1* or *dynein2* (Dharmacon Smart Pool; sequences available on request) were also used. Control siRNA was described previously (*GFP*, lamin[39]). The efficacy of *dynein1* and *dynein2* knockdown was assessed by PCR with reverse transcription (DYNC1H1 forward: 5′-GGAAGTCAACGTCACCACCT-3′; DYNC1H1 reverse: 5′-CCAACCTCAGACCAACCACT-3′; DYNC2 forward: 5′-GTCAGCTGGAGGAAGACTGG-3′; DYNC2 reverse: 5′-GCACCAACAATTTTGT-CACG-3′; glyceraldehyde 3-phosphate dehydrogenase (GAPDH) forward: 5′-CGACCACTTTGTCAAGCTCA-3′; GAPDH reverse: 5′-AGGGGAGATTCAGTG-TGGTG-3′) using a OneStep RT–PCR kit (QIAGEN) for both *dynein1* and *dynein2* and by western blot for dynein1. Functional assays for loss of dynein1 and dynein2 were done 48 h and 72 h post-transfection and included Golgi fragmentation (dynein1 and dynein2) and mitosis-related (dynein1) or cilia assays (dynein2) previously described[39].

Zebrafish lines, morpholino injection and phenotyping. Wild-type zebrafish were raised according to standard protocols[40]. 1-phenyl-2-thiourea (PTU, Sigma) was used to suppress pigmentation when necessary, according to standard protocols[40]. Embryos were staged according to hours post-fertilization (hpf). IFT88 morpholino antisense oligonucleotides (IFT88 morpholino oligonucleotides: 5′-CTGGGACAAGATGCACATTCTCCAT-3′) were previously described[18] and standard control morpholino oligonucleotides were used. The efficacy of IFT88 morpholino oligonucleotides injection was assessed by changes in gross anatomical features (for example, curly trunk and pronephric duct defects, cyst formation) characteristic of IFT88 zebrafish mutants[4,18]. Gross anatomical defects and cyst formation were observed in 32 hpf and 52 hpf embryos, with a MZFLIII dissection microscope (Zeiss). One-cell-stage embryos were injected with 10 ng of control or IFT88 morpholino oligonucleotides as previously described[18]. Embryos at 52 hpf were used for whole-mount staining or flow cytometry (see below).

Antibodies. The following antibodies were used: IFT88 (from G. Pazour or Proteintech for biochemistry; western blot, 1:500, immunoprecipitation, 5 μg; or from C. Desdouets, Faculte de Medecine Rene Descartes, Paris; immunofluorescence 1:250); IFT20 (G. Pazour, western blot 1:500); IFT52 (western blot 1:500, Proteintech); polyglutamylated tubulin antibody (GT335, P. Denoulet, UMR7622, Paris, France and C. Janke, Institut Curie, France; immunofluorescence, 1:500); α-tubulin (DM1 α, immunofluorescence, 1:250), FITC-conjugated α-tubulin (1:300), γ-tubulin (western blot, 1:500; immunofluorescence, 1:250), EB1 (immunofluorescence, 1:250; immunoprecipitation, 5 μg), BrdU (1:250), Flag (western blot, 1:500; immunoprecipitation, 5 μg) and acetylated tubulin (1:250) from Sigma; Ser 10 Phos-H3 (1:500, Upstate Biotechnology); EB1 (western blot, 1:300; immunofluorescence, 1:250), p150/glued (western blot, 1:1,000) and p50/dynactin (western, 1:500) from BD Biosciences; dynein intermediate chain 74.1 (immunofluorescence, 1:250; western blot, 1:500, immunoprecipitation, 5 μg, Santa Cruz Biotechnology); Golgin 97 (immunofluorescence, 1:250, Molecular Probes); and CREST (immunofluorescence, 1:250 anti-human centromere/kinetochore; Antibodies Inc.). 5051 (immunofluorescence, 1:500) has been described previously[39].

Lysates, cell synchronization, immunoprecipitation and gel filtration. Cell lysates were obtained from HeLa cells 48 h or 72 h post siRNA transfection. Lysis buffer: 50 mM HEPES (pH 7.5), 150 mM NaCl, 1.5 mM $MgCl_2$, 1 mM EGTA, 1% IGEPAL CA-630 and protease inhibitors (Complete Mini, Roche Diagnostics). Protein concentration for lysate was determined using Bio-Rad protein dye reagent (Bio-Rad Laboratories), loads were adjusted, proteins were resolved by SDS–PAGE, and analysed by western blotting. Cell synchronization for biochemistry was achieved using double thymidine block in HeLa cells (2 mM, 20 h) and release (10 h) to achieve mitotic enrichment followed by mitotic shake off. IMCD cells were synchronized in mitosis using R0-3306 inhibitor (reversibly arrests cells at the G_2-M border, Enzo Life Sciences AG) overnight then released for 1 h. For immunoprecipitation, antibodies were added to cell extracts and incubated at 4 °C overnight, and then incubated for 45 min with protein G-PLUS agarose (Santa Cruz Biotechnology). Immunoprecipitated proteins were separated by SDS–PAGE and analysed by western blotting. For gel filtration, mitotic cell lysates (lysis buffer: 20 mM HEPES at pH 7.6, 5 mM $MgSO_4$, 0.5 mM EDTA, 50 mM KCl and 1% NP-40; volume: 0.250 ml; protein concentration: 12 μg μl^{-1}) were loaded onto a fast protein liquid chromatography Superose 6 gel-filtration column (GE Healthcare; 0.2 ml min^{-1}, equilibrated in extraction buffer), and 0.5 ml fractions were collected.

Flow cytometry. For flow cytometry, 52 hpf zebrafish embryos were grown in egg water and dechorionated by pronase treatment[40], rinsed for 15 min in calcium-free Ringer and passed several times through a 200 μl pipette tip to remove the yolk. Embryos were transferred into a 35 mm culture dish with 2 ml phosphate buffered saline (PBS, at pH 8) containing 0.25% trypsin and 1 mM EDTA and incubated for 30–60 min at 28.5 °C. The digest was stopped by adding $CaCl_2$ to a final concentration of 1 mM and fetal calf serum to 10%. Cells were centrifuged for 3 min at 300*g*, rinsed once with PBS and fixed and processed for flow cytometry. Cells were stained for flow cytometry experiments as previously described[39]. Phos-H3 staining (Ser 10 Phospho-Histone 3, Alexa Fluor 488 conjugate), was carried out according to manufacturers' instructions (Cell Signaling).

Microtubule binding assay. Mitotic cells were lysed at 4 °C in 100 mM 1,4-piperazinediethanesulphonic acid, at pH 6.8, 1 mM $MgCl_2$, 2 mM EGTA and 1% Triton X-100, and spun at 13,000*g* for 30 min. Microtubule affinity experiments were carried out as described previously[32] with some modifications. Briefly, purified tubulin (10 μg), dithiothreitol (1 mM), GTP (1 mM) and taxol (10 μM) were added to cleared lysates, and incubated for 1 h at 37 °C. Nocodazole (10 μM) was added as a negative control. Lysates were layered over a 20% sucrose cushion in the above buffer and spun at 100,000*g* for 1 h at room temperature. Microtubule pellets were collected after removing lysate and cushion, and bound proteins were separated by SDS–PAGE and analysed by western blotting.

Microtubule regrowth assay. At 48 h post-transfection, microtubules were depolymerized in 10–25 μM nocodazole in culture medium for 1 h at 37 °C. Cells were then washed and incubated in culture medium without nocodazole at 37 °C to allow regrowth. Cells were fixed at different time intervals in methanol and processed for immunofluorescence microscopy to examine microtubule regrowth (α-tubulin) from spindle poles in metaphase cells.

Immunofluorescence experiments, microscopy and imaging software. Whole embryos (48 h) were processed for immunofluorescence by fixation in Dent's Fix (80% methanol/20% dimethylsulphoxide) at 4 °C overnight, rehydrated, washed with PBS containing 0.5% Tween 20 (PBST), and blocked in 1× PBS-DBT (1% dimethylsulphoxide, 1% BSA, 0.5% Tween 20) at room temperature for 2 h. Primary and secondary antibody incubations were carried out in 1× PBS-DBT at 4 °C overnight and 1 h at room temperature, respectively, using 1× PBS-DBT washes between incubations. After rinsing in 1× PBS, the embryos were mounted and examined using a Perkin Elmer Ultraview spinning disc confocal microscope: Zeiss Axiovert 200M, ×100 Plan-Apocromat NA 1.4 Oil objective, or ×63 Plan-Apocromat NA 1.4 Oil objective and Hamamatsu ORCA-ER camera. Images were processed on a MetaMorph workstation (Molecular Devices). *Z* stacks were acquired and used for creation of maximum projections or (3D) rendering (below).

Immunofluorescence microscopy analysis of −20 °C methanol-fixed cells was carried out as previously described[39]. Images were acquired using the spinning disc confocal microscope described above (×100 Plan-Apocromat NA 1.4 Oil objective). *Z* stacks were shown as 2D maximum projections (MetaMorph) or processed for 3D rendering (Imaris, Bitplane). Fluorescence range intensity was adjusted identically for each series of panels. Intensity profiles, linescan histograms and fluorescence intensity quantification were obtained from sum projections of *Z* stacks using MetaMorph. For fluorescence intensity quantification, computer-generated concentric circles of 60 (inner area) or 80 (outer area) pixels in diameter were used to measure spindle pole (inner area) and calculate local background (difference between the outer and inner area) fluorescence intensity. Imaris 3D rendering software was used to visualize spindle orientation and to measure distances required to calculate spindle angle. Spindle angle measurements were carried out as previously described[15].

Time-lapse microscopy imaging. Time-lapse microscopy imaging of cultured HeLa cells was carried out using the spinning disc microscope described above (×25 Plan-Neofluar NA 0.5, phase) using the scan stage tool (MetaMorph). Images were taken every 10 min from 32 h to 48 h post-transfection. For live microscopy of GFP–EB1 in metaphase HeLa cells, images were recorded every 5 s for 2 min using the spinning disc confocal microscope described above (×63 Plan-Apocromat

DOI: 10.1038/ncb2202

NA 1.4 Oil objective). Microtubule-nucleation rate was measured in GFP–EB1-expressing cells by manually counting the number of EB1–GFP comets emerging from the centrosome over time. For live microscopy of GFP–IFT88 in metaphase, single-plane images were recorded once per second using the spinning disc confocal microscope described above (×100 Plan-Apocromat NA 1.4 Oil objective). The resulting movie is shown at 3 frames per second. Tracking of IFT88 foci was obtained using the track point application in MetaMorph. Live imaging of the GFP–α-tubulin LLC-PK1 cell line was carried out as previously described[21]. Resulting movies are shown at 10 frames per second.

Statistical analysis. The number of embryos or cells counted per experiment for statistical analysis is indicated in figure legends. For graphs in all figures: error bars, mean of at least 3 experiments ± s.d. unless otherwise specified; *n*, number of events per experiment. Images: scale bars, 5 μm unless otherwise specified. Graphs were created using GraphPad Prism software.

37. Pazour, G. J., San Agustin, J. T., Follit, J. A., Rosenbaum, J. L. & Witman, G. B. Polycystin-2 localizes to kidney cilia and the ciliary level is elevated in orpk mice with polycystic kidney disease. *Curr. Biol.* **12,** R378–R380 (2002).
38. Follit, J. A., Xu, F., Keady, B. T. & Pazour, G. J. Characterization of mouse IFT complex B. *Cell Motil Cytoskeleton* **66,** 457–468 (2009).
39. Mikule, K. *et al*. Loss of centrosome integrity induces p38-p53-p21-dependent G1-S arrest. *Nat. Cell Biol.* **9,** 160–170 (2007).
40. Westerfield, M. *The Zebrafish book : a guide for the laboratory use of zebrafish (Brachydanio rerio)* (Univ. Oregon Press, 1993).

nature cell biology

DOI: 10.1038/ncb2202

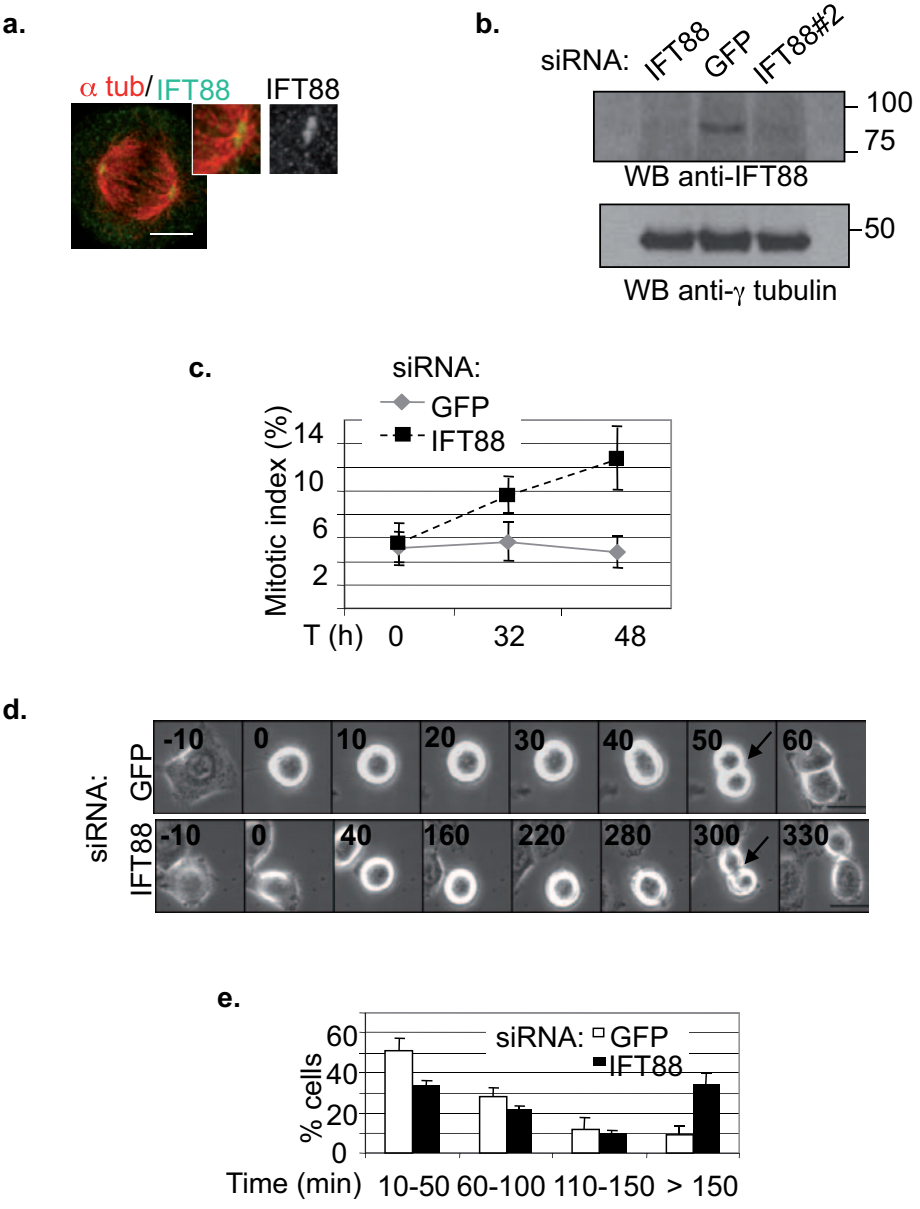

Figure S1 IFT88 depletion leads to mitotic defects in HeLa cells. **(a)** Immunofluorescence images of IFT88 at spindle poles in a metaphase HeLa cell. Enlargements, spindle pole. Scale bar, 5μm. **(b)** Western blot showing IFT88 depletion in HeLa cells using two independent siRNAs. GFP, control siRNA; γ tubulin, loading control. **(c)** Manual counts of mitotic indices of control (GFP) and IFT88 depleted HeLa cells 0h, 32h and 48h after transfection. n=500 cells/experiment. h, hours. **(d, e)** Time-lapse imaging of HeLa cells (d) showing progression from nuclear envelope breakdown (NEB, 0 min) to anaphase onset (arrows, first frame following anaphase onset). siRNA treatment as indicated. Time in minutes (min). Graph (e): Time required for cells to progress from NEB to anaphase onset, percentage of cells for each time interval. n=100 mitotic cells from two independent experiments.

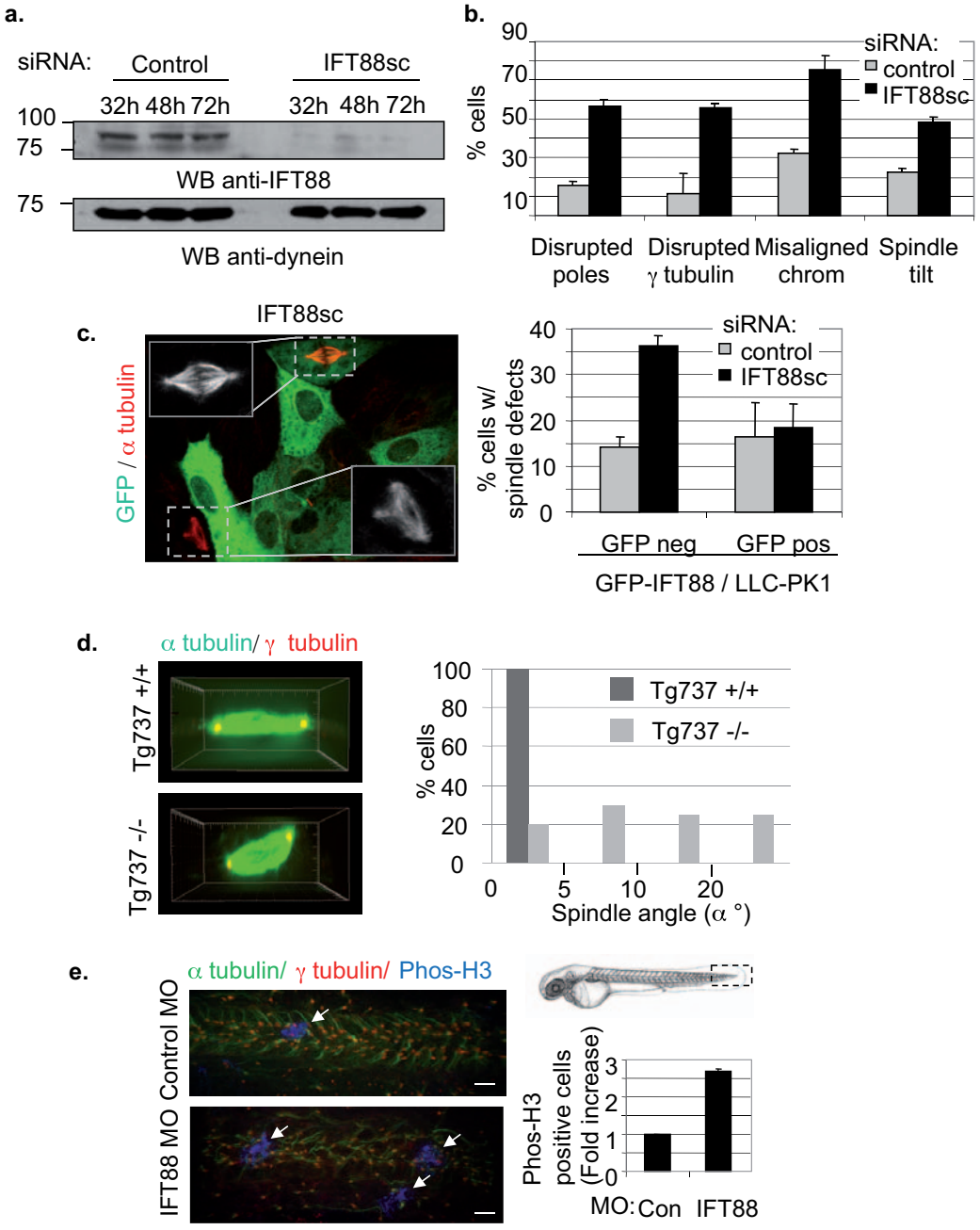

Figure S2 IFT88 depletion leads to mitotic defects in kidney cells and zebrafish. **(a, b)** Western blot (a) showing IFT88 depletion in GFP-α tubulin LLC-PK1 cells. IFT88 siRNA designed against pig (IFT88sc, *Sus Scrofa*) IFT88 sequence. Dynein, loading control. Time, hours after siRNA transfection. Quantification (b) of GFP-α tubulin LLC-PK1 cells with mitotic defects following IFT88 or control (lamin) siRNA treatment. Defects include disrupted poles (α tubulin), disrupted γ tubulin, misaligned chromosomes (DAPI) or spindle misorientation (spindle tilt). n=70 mitotic cells/experiment. **(c)** Depletion of endogenous IFT88 (pig siRNA) in LLC-PK1 cells is rescued by the expression of GFP-IFT88 (mouse cDNA). Immunofluorescence images (left) of the GFP-IFT88 expressing LLC-PK1 cell line treated with IFT88sc siRNA. Normal spindle in a cell expressing GFP-IFT88; disrupted spindle in a GFP negative cell. Corresponding quantification (right) showing that, in the GFP-IFT88 LLC-PK1 cell line, depletion of endogenous IFT88 leads to an increase in spindle defects in cells that are GFP-IFT88 negative but not in cells that are GFP-IFT88 positive. Lamin, siRNA control. **(d)** Side views of three-dimensional reconstructed immunofluoresence images (left) show misoriented mitotic spindles in kidney cells derived from the IFT88 mouse mutant *Tg737*^{orpk} (*Tg737-/-*) compared to *Tg737+/+* cells. Histogram (right) shows metaphase spindle angle distribution. n=35 mitotic spindles. **(e)** Immunofluorescence images of phos-H3 positive mitotic cells in tail buds of whole mount control or IFT88 depleted zebrafish embryos reveals an increase in mitotic cells. Schematic representation (top right) shows the corresponding tail bud region. Arrows, mitotic cells. MO, morpholino. Graph (right): Quantification by flow cytometry of mitotic phos-H3 positive cells obtained from dissociated embryos. n=30 embryos/experiment. n>20,000 total cells/experiment. For graphs in all panels: error bars, mean of at least 3 experiments ± SD unless otherwise specified.

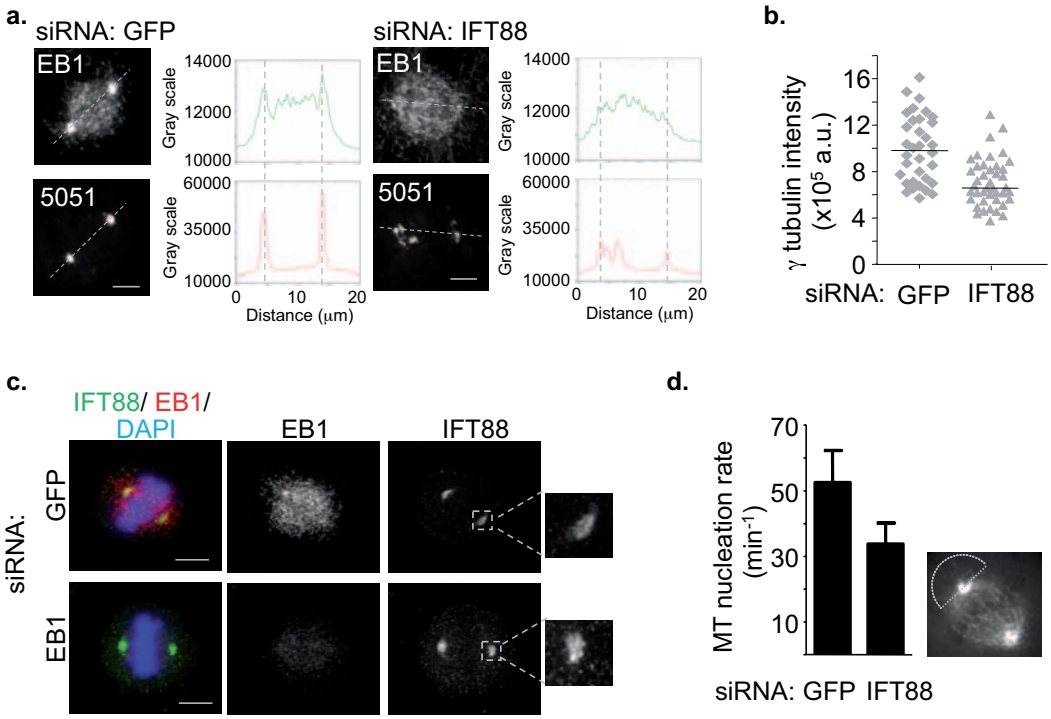

Figure S3 IFT88 depletion disrupts the spindle pole localization of EB1 and gamma tubulin thus decreasing MT nucleation at spindle poles, whereas EB1 depletion does not disrupt spindle pole localization of IFT88. **(a)** Images of mitotic spindles and corresponding linescan histograms showing selective loss of EB1 from poles but not from spindles in IFT88-depleted HeLa cells versus control cells. **(b)** Quantification of γ tubulin intensity at spindle poles in GFP- and IFT88-siRNA treated HeLa cells. a.u., arbitrary unit. **(c)** Immunofluorescence images show that EB1 depletion does not affect IFT88 localization at spindle poles of HeLa cells despite EB1 loss from spindle (bottom panel, middle). Right, pole enlargements. **(d)** MT nucleation rate was measured in HeLa cells transiently expressing EB1-GFP by counting the number of EB1-GFP comets emerging from the centrosome over time. n= 8 cells for control; n=5 cells for IFT siRNA. Nucleation rate was measured for the astral side of the centrosome, as outlined by the white half-circle on the EB1-GFP image of a mitotic cell (right). Error bars, mean of at least 3 experiments ± SD.

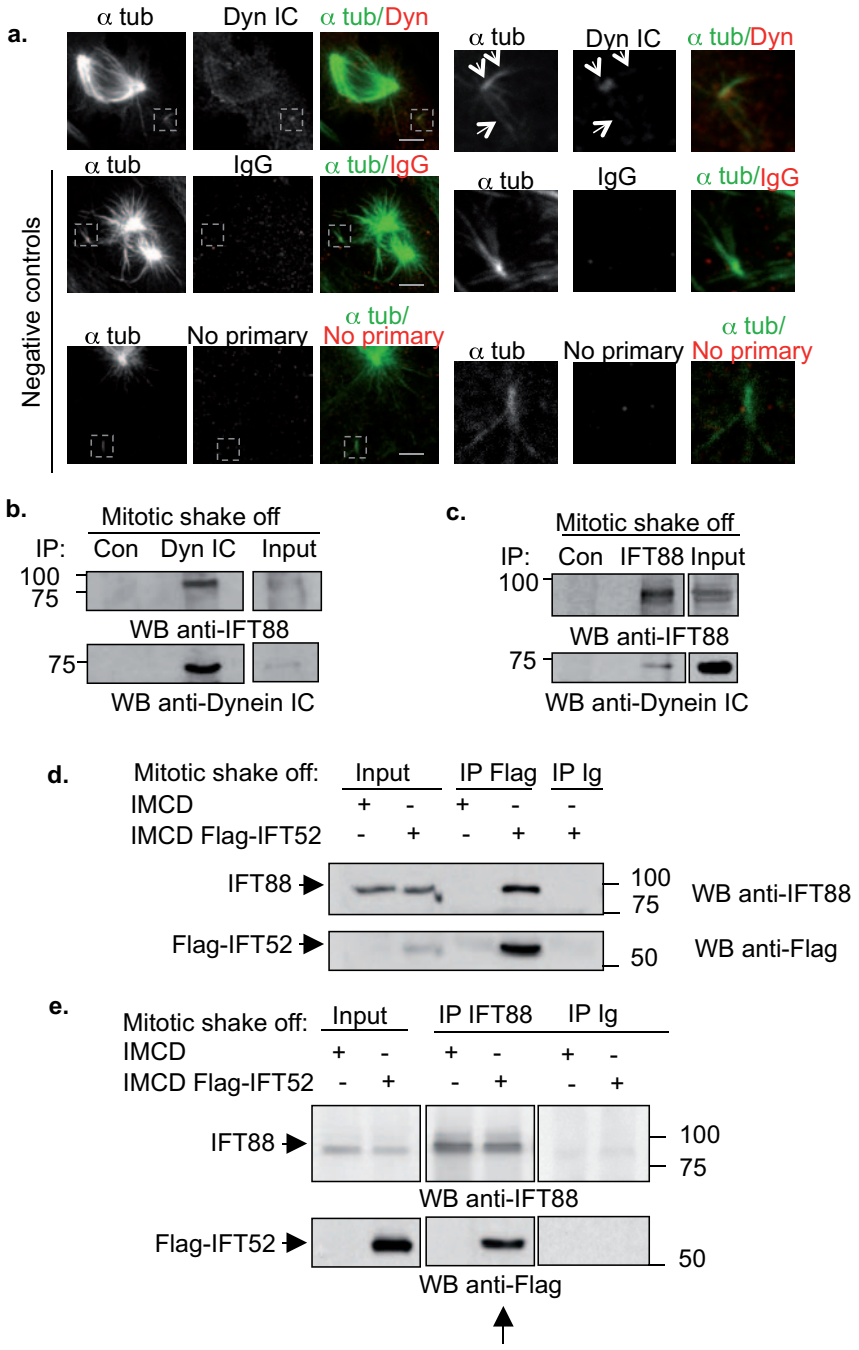

Figure S4 IFT88 colocalizes with dynein in MT clusters in prometaphase and interacts with dynein and Flag-IFT52 in mitotic cells. **(a)** Immunofluoresence images showing dynein (intermediate chain, dynein IC) localizing at the minus end of a peripheral MT cluster and along the MTs of the cluster (arrows) in a prometaphase cell. Scale bar, 5μm. Inset, peripheral MT cluster. GFP-αtubulin, MTs. Negative controls, mouse IgG and no primary antibody. **(b-c)** Immunoblots showing that (b) IFT88 co-immunoprecipitates with cytoplasmic dynein intermediate chain from mitotic HeLa cells lysates, and (c) that cytoplasmic dynein intermediate chain co-immunoprecipitates with IFT88 from lysates of mitotic HeLa cells. Negative IP control (Con), Ig, mouse or rabbit antibody. Input, 5% of total lysate used for IP. **(d)** Immunoblots showing that IFT88 co-immunoprecipitates with Flag-IFT52 from mitotic lysates of inner medullary collecting duct (IMCD) cells stably expressing Flag-IFT52. Ig mouse antibody, negative IP control. Input, 5% of total lysate used for IP. **(e)** Immunoblots showing Flag-IFT52 co-immunoprecipitating with IFT88 from mitotic lysates of IMCD cells stably expressing Flag-IFT52. Ig, rabbit, negative IP control. WB, Western Blots as indicated. IP, immunoprecipitation. Input, 5% of total lysate used for IP. For full scan of immunoblots see Supplementary Fig. S8.

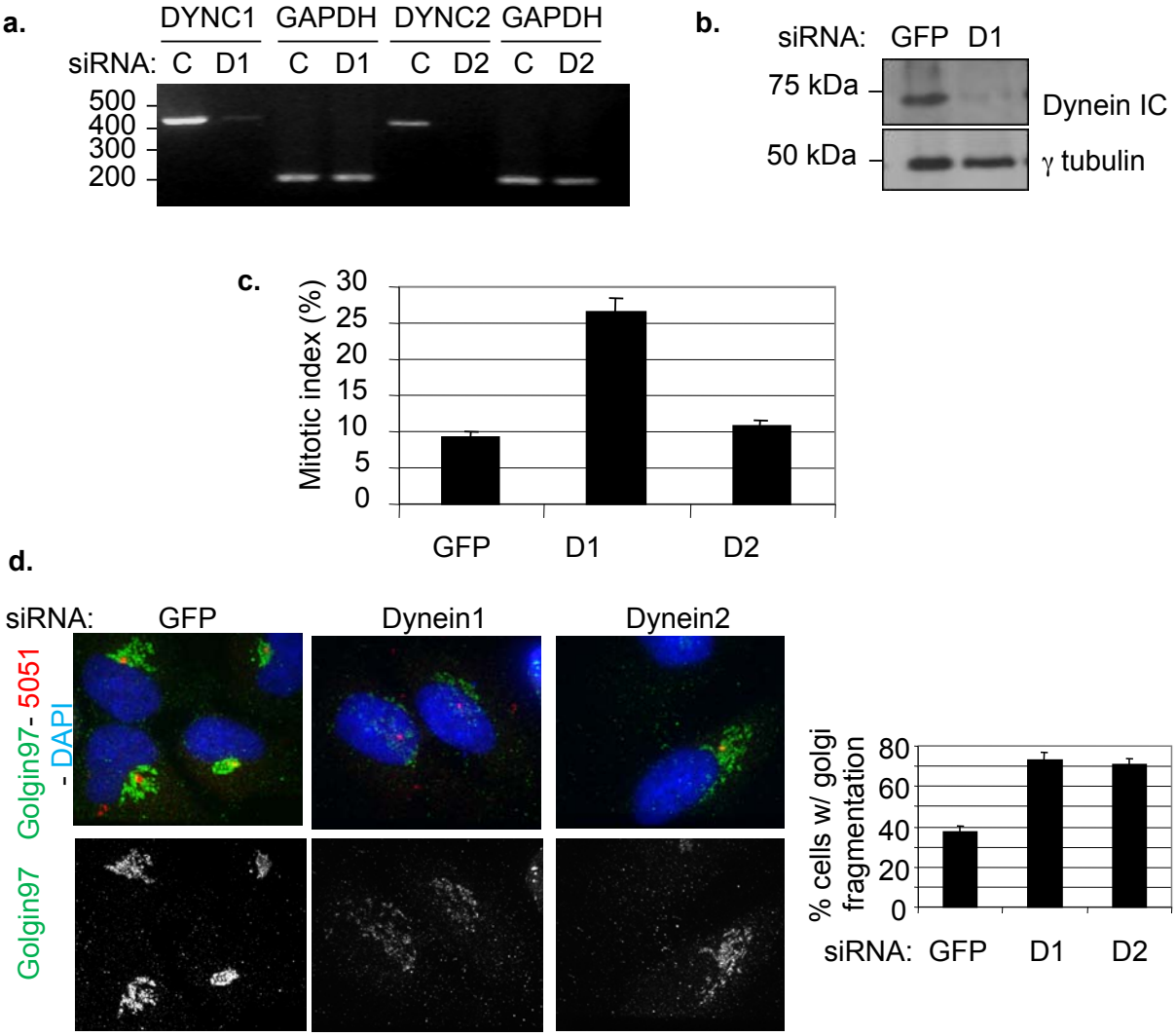

Figure S5 Depletion of dynein1 heavy chain but not dynein 2 disrupts mitosis whereas depletion of either disrupts interphase in HeLa cells. **(a)** RT-PCR shows loss of cytoplasmic dynein1 mRNA (oligo, DYNC1) after siRNA depletion of the heavy chain of cytoplasmic dynein1 (D1) compared to GFP control (C) and loss of cytoplasmic dynein2 mRNA (oligo, DYNC2) after siRNA depletion of the heavy chain of cytoplasmic dynein2 (D2) compared to GFP control siRNA (C); GADPH, loading control. **(b)** Immunoblot from lysates of HeLa cells treated with cytoplamic dynein1 heavy chain (D1) siRNA shows decrease in the intermediate chain subunit of the complex (dynein IC) compared to control (GFP). γ tubulin, loading control. **(c)** Manual counting of mitotic indices after GFP, dynein1 (D1) or dynein2 (D2) siRNA in HeLa cells showing that dynein1 but not dynein2 depletion induces an increase in mitotic index. n=250 cells/ experiment. **(d)** Immunofluorescence images of dynein1 (D1) and dynein2 (D2) depleted HeLa cells show that both dynein1 and dynein2 depletion result in previously reported interphase phenotypes. The previously reported golgi fragmentation (golgin 97) following dynein depletion functionally confirms the efficacy of both siRNAs. Graph (right), quantification of cells with golgi fragmentation. Error bars, mean of at least 3 experiments ± SD, n=230 cells/ experiment.

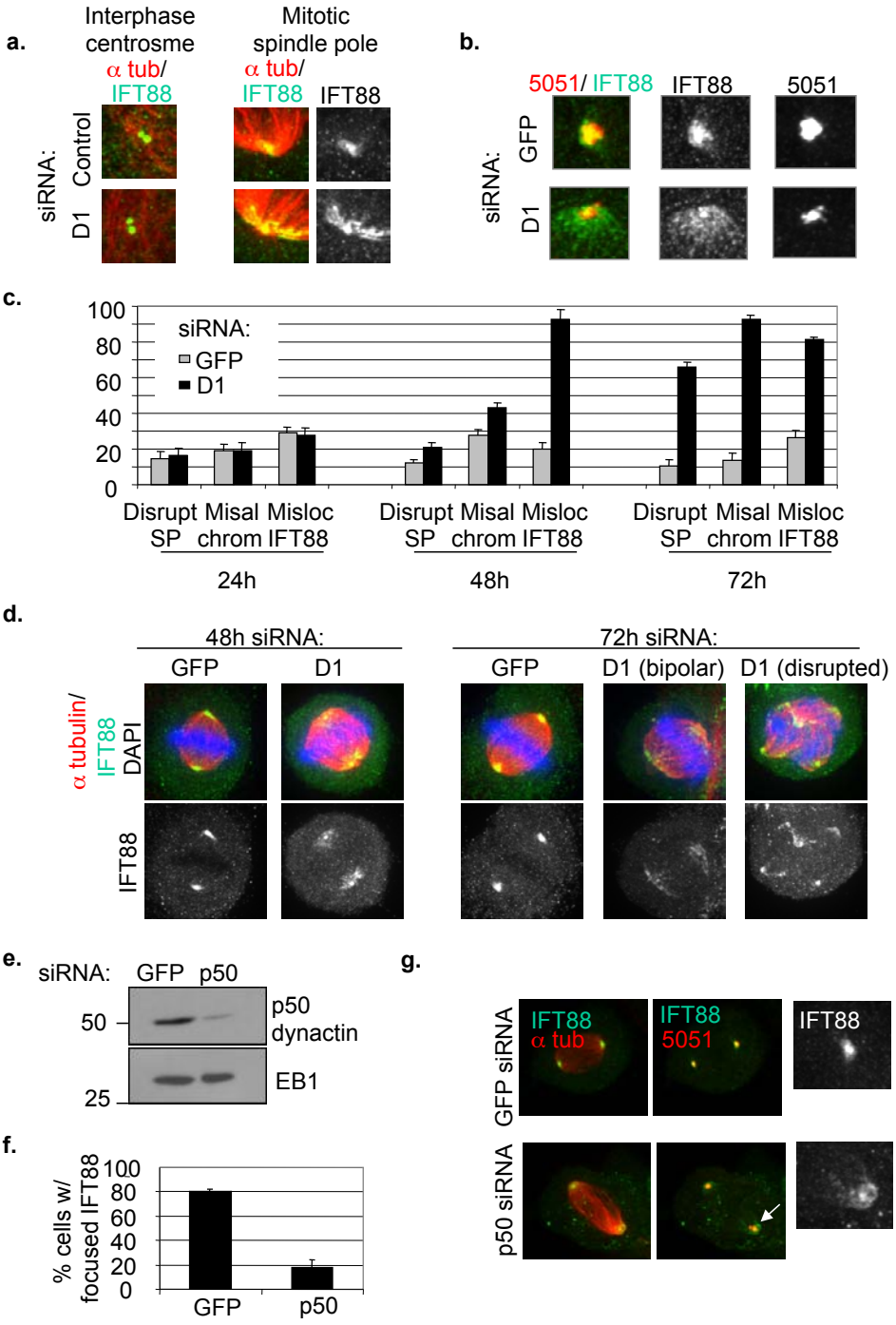

Figure S6 Dynein1 and p50 depletion disrupts the spindle pole localization of IFT88 in HeLa cells. **(a)** Immunofluoresence images showing that Dynein1 (D1) depletion leads to major disruption of the localization of IFT88 at spindle poles (right panels) but no major disruption is observed at interphase centrosomes (left panels) as previously reported (Robert et al., 2007). **(b)** Immunofluoresence images showing that the centrosome marker 5051 is decreased but not defocused in D1 depleted mitotic cells demonstrating the specificity of IFT88 redistribution. **(c)** Early (24h, 48h after transfection) and late (72h after transfection) time points following D1 depletion reveal that IFT88 mislocalization (misloc.) occurs before major spindle disruption (disrupt SP) including misaligned chromosomes (misal. chrom.). **(d)** Corresponding immunofluorescence images. **(e)** Western blots showing loss of p50 dynactin 48h after transfection. GFP, siRNA control. EB1, loading control. **(f)** Quantification, % cells with disrupted IFT88 pole localization in p50 depleted cells compared to control (GFP). Average of 3 independent experiments ± SD. n=60 mitotic spindles. **(g)** Mitotic spindles (α tubulin) showing loss of focus of IFT88 at spindle poles (arrow) in p50 dynactin depleted HeLa cells. 5051, spindle pole. Enlargements, spindle poles.

a.

siRNA: / Functional assay:	GFP	D1	D2
Increased mitotic index	no	yes	no
IFT88 accumulation around spindle poles (unfocused staining)	no	yes	no
Golgi fragmentation	no	yes	yes
IFT88 accumulation at the tip of cilium	no	no	yes

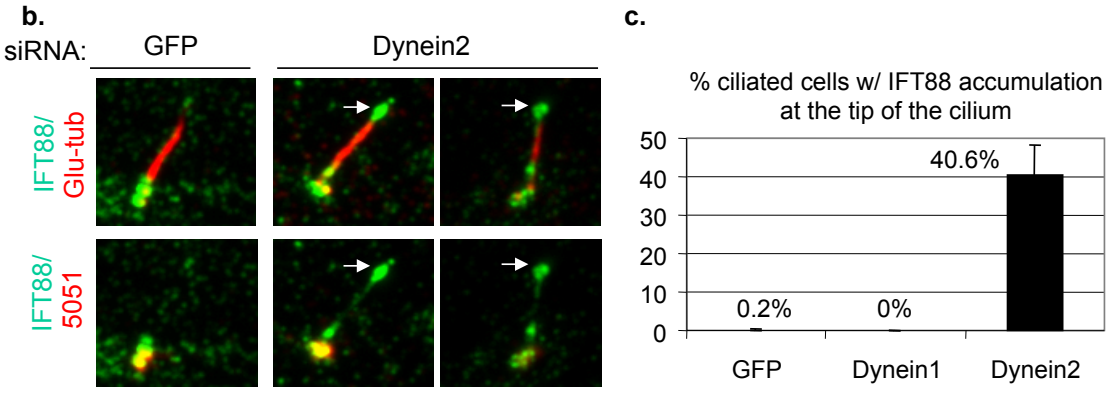

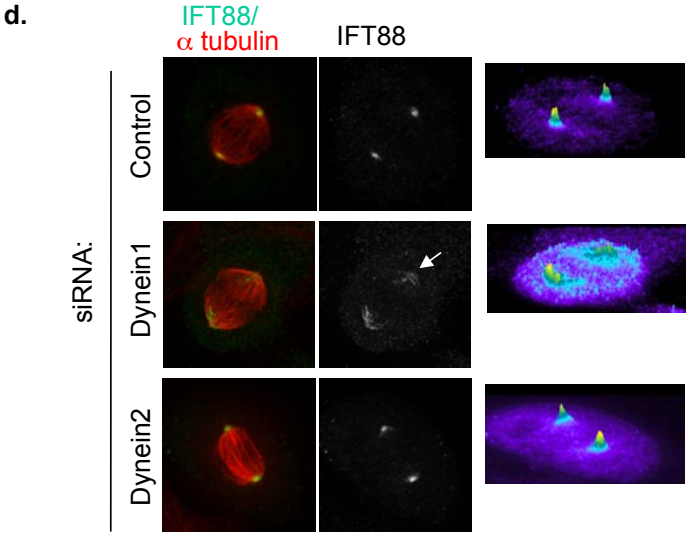

Figure S7 Dynein2 depletion causes IFT88 accumulation at tips of cilia but does not disrupt IFT88 localization at spindle poles **(a)** Summary table of dynein1 (D1) and dynein2 (D2) siRNA functional assays in mitotic cells (two top rows) and interphase cells (two bottom rows). **(b)** Immunofluoresence images showing redistribution and accumulation of IFT88 at the tip of the cilium (arrow) in RPE serum-starved cells following dynein2 depletion, functionally confirming the efficacy of the siRNA. Polyglutamylated tubulin, cilium. 5051, basal body. **(c)** Quantification of defects in ciliated RPE cells after GFP, dynein1 or dynein2 siRNA. Average of 3 independent experiments +/- SD, n=225 ciliated cells. **(d)** Mitotic spindles of HeLa cells stained for microtubules (α tubulin) and IFT88 showing disrupted IFT88 localization at spindle poles (arrow) in dynein1 but not dynein2 or control depleted cells. Inset (right), IFT88 intensity profiles.

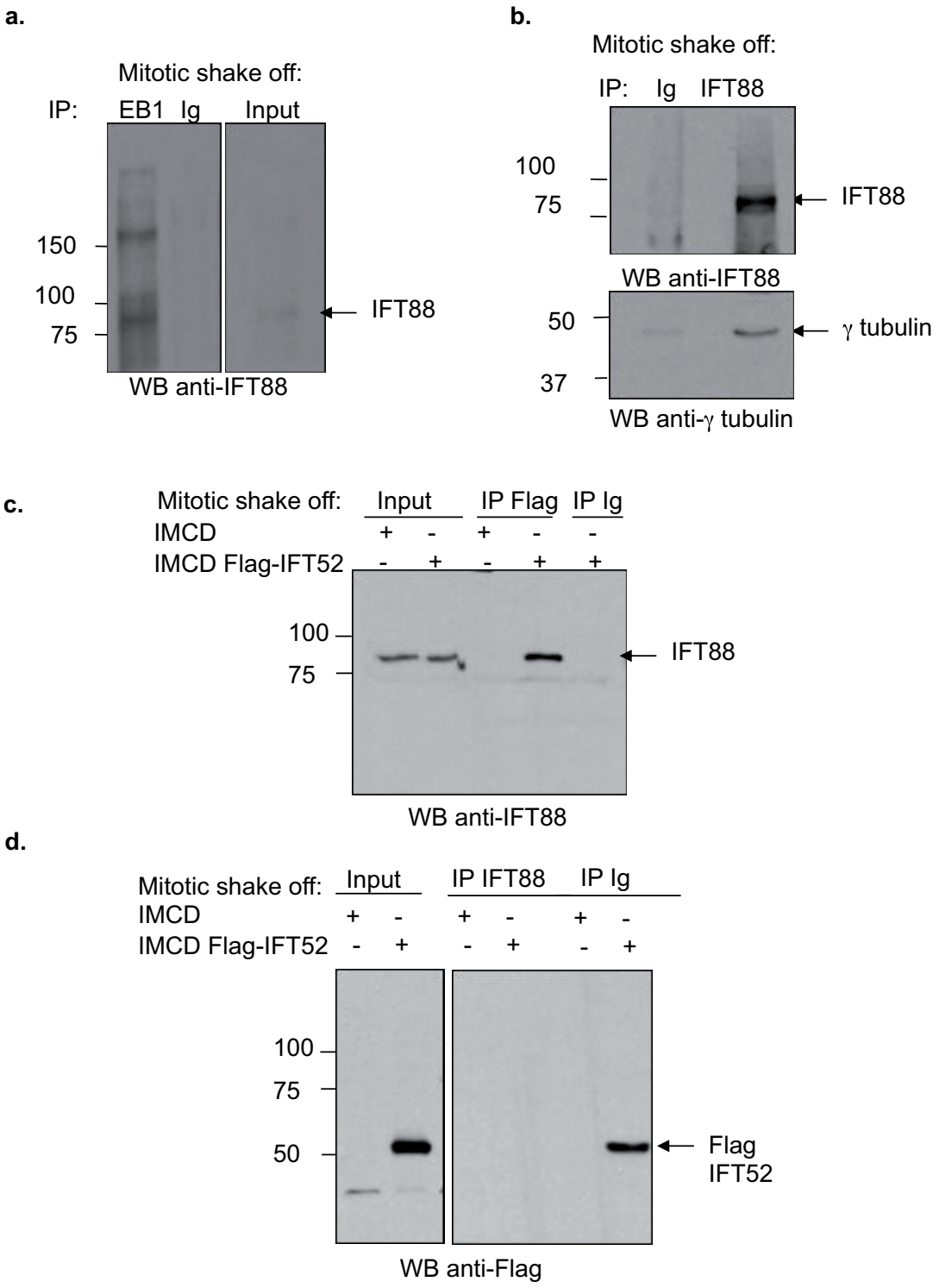

Figure S8 Full scans of key immunoblots. **(a)** IFT88 immunoblots of EB1 immunoprecipitation and total lysate (input). Shown in Fig. 2e. **(b)** γ tubulin and IFT88 immunoblots of IFT88 immunoprecipitation. Shown in Fig. 2e. **(c)** IFT88 immunoblot of Flag immunoprecipitation and total lysate (input). Shown in Supplementary information figure S4d. **(d)** Flag immunoblots of IFT88 immunoprecipitation and total lysate (input). Shown in Supplementary information figure S4e. **(e)** Immunoblots using antibodies as indicated of gel filtration fractions and input. Shown in Fig. 5a. Dotted lines indicate where membrane was cut before blotting. **(f)** IFT88 and dynein IC immunoblots of dynein IC immunoprecipitation and total lysate (input). Shown in Fig. 5a.

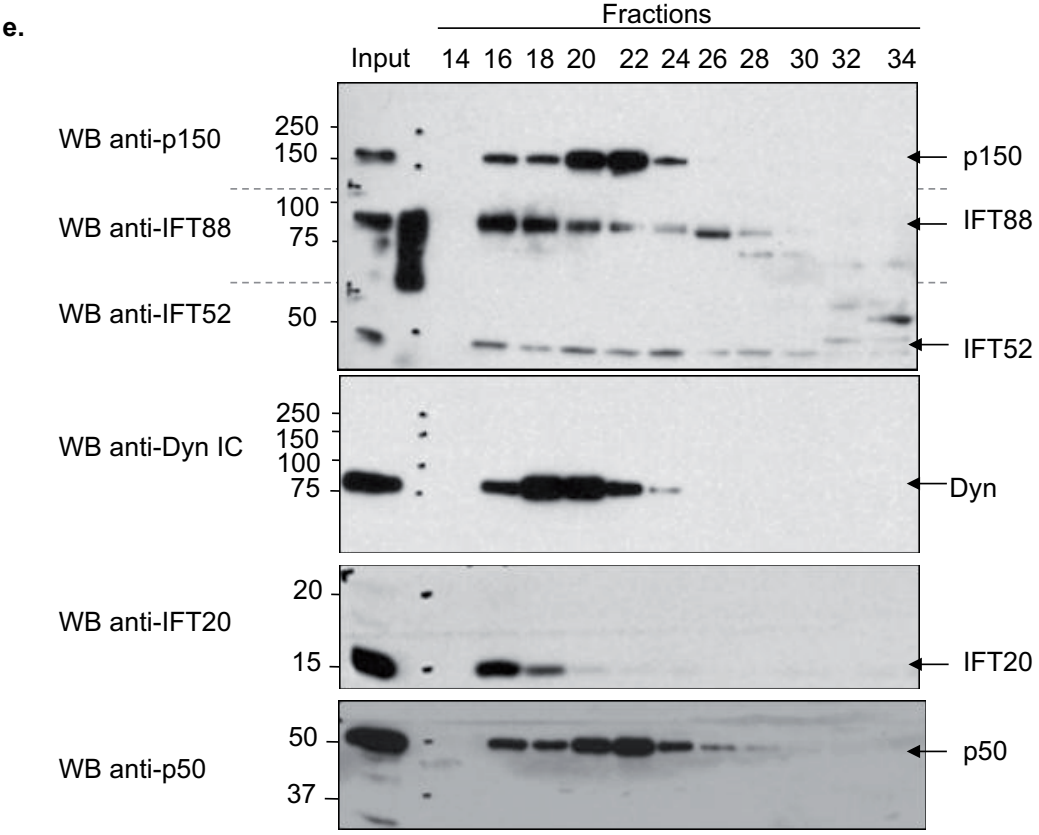

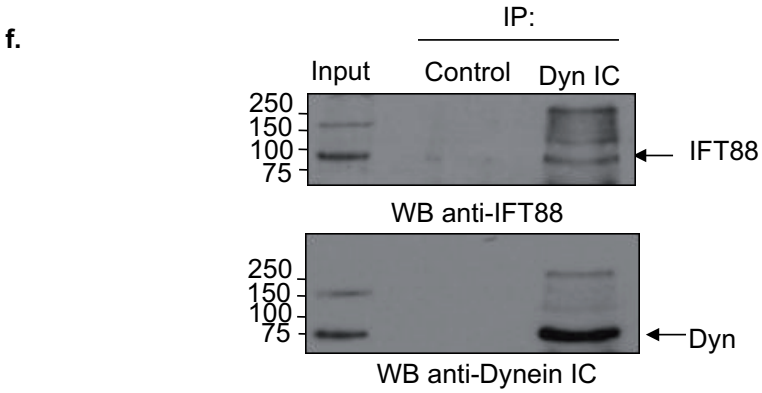

Figure S8 continued

Supplementary movie legends

Movie S1 Time-lapse movie of a control GFP-α tubulin LLC-PK1 prometaphase cell showing minus-end directed motion of peripheral MT clusters (arrows) toward spindle pole.

Movie S2 Time-lapse movie of a control GFP-α tubulin LLC-PK1 metaphase cell showing minus-end directed motion and subsequent integration of a peripheral MT cluster (arrow) into a spindle pole.

Movie S3 Time-lapse movie of an IFT88-depleted GFP-α tubulin LLC-PK1 prometaphase cell showing peripheral MT clusters accumulation in the cytoplasm. These clusters (arrow) are not moving toward spindle poles.

Movie S4 Time-lapse movie of an IFT88-depleted GFP-α tubulin LLC-PK1 metaphase cell, showing a peripheral MT cluster not moving toward spindle pole.

Movie S5 Time-lapse movie of a GFP-IFT88 LLC-PK1 metaphase cell showing one of the IFT88 foci (arrow) moving toward a spindle pole.